Spatially resolved modelling of NH_3 cracking in warm plasma

Rubén Quiroz Marnef*[1], Stein Maerivoet*[1,2], Ivan Tsonev[1], François Reniers[2] and Annemie Bogaerts[1]

[1] Research group PLASMANT, Department of Chemistry, University of Antwerp, Universiteitsplein 1, BE-2610 Wilrijk-Antwerp, Belgium

[2] Chemistry of Surfaces, Interfaces and Nanomaterials, Faculty of Sciences, Université Libre de Bruxelles, CP255, Avenue F.D. Roosevelt 50, B-1050 Brussels, Belgium

* These authors contributed equally to the work

E-mail: ruben.quirozmarnef@uantwerpen.be; stein.maerivoet@uantwerpen.be; annemie.bogaerts@uantwerpen.be

Abstract

We developed a fully coupled 2D axisymmetric model for NH_3 cracking in a warm low-current arc pin-to-pin plasma reactor, by solving the equations of gas flow dynamics, heat transfer, electric currents, and chemistry. The full chemistry is first reduced to a set of 12 species and 23 reactions, feasible to solve in a 2D model. Our model was validated by experiments over a wide range of electric currents (2-180 mA), flow rates (5-20 NLM), and different interelectrode gap distances (3-5 cm). This ensures we explore a significant range of specific energy input (SEI = 7-55 kJ/mol). As our model yields excellent agreement with experimental results, we can use it to understand the underlying physics and chemistry. The conversion happens predominantly in a narrow chemically active region with gas temperatures between 2400 and 3000 K. Importantly, the conversion is determined by the transport of NH_3 and H atoms to this region. Furthermore, our model reveals that thermal chemistry is dominant for NH_3 cracking in warm plasmas. The calculated energy cost is around 200 kJ/mol, and remarkably constant over a wide range of SEI. Finally, we identified that 60-64 % of the deposited energy is lost as residual heat, limiting the achievable energy efficiency. Overall, our study helps to better understand the mechanisms of NH_3 cracking in warm plasma, and what is needed to improve the performance, and can thus be used as a steppingstone for improved reactor design.

Keywords:
Plasma, predictive modelling, 2D models, CFD, pathway analysis, NH3 cracking, green hydrogen production

1 Introduction

Hydrogen gas (H_2) is a main driver in the decarbonization plans of the European Union[1]. It can also play a crucial role in achieving sustainable development goal 7 of the United Nations for 'affordable and clean energy'[2]. However, efficient transport remains an issue due to the low volumetric energy density and relatively high costs[3]. A wide range of possible solutions to this transport problem is under investigation, from compressing or condensing H_2 gas, to transforming it to other chemicals that are easier and/or safer to transport[4]. One of the main promising chemical carriers is NH_3, due to its high volumetric weight density. However, more efficient and sustainable NH_3 cracking methods are needed.[5] NH_3 cracking ideally only produces the useful H_2 gas and the harmless byproduct of N_2 gas. The overall (endothermic) chemical reaction is:

$$2\,NH_3 \rightleftharpoons N_2 + 3\,H_2 \qquad \Delta H° = 91.8\,kJ \qquad (1)$$

NH_3 thermocatalytic cracking installations already exist in pilot phase since 2023, and they achieve an energy cost (EC) of 102 kJ/mol[6]. Note that this EC, and throughout this work, is per mole of NH_3. Ru is the most active catalyst for NH_3 cracking. It fully dissociates NH_3 at temperatures higher than 500 °C[7]. While catalytic crackers remain the most important avenue of research,[6,8] an emerging fully electrified method is plasma-assisted NH_3 cracking[9]. Indeed, plasma can rapidly be turned on/off, making it suitable for a fluctuating renewable energy grid. This approach has gained increased attention in the last years, both utilizing dielectric barrier discharge (DBD)[10–12] and warm plasmas[13–18]. The best performing DBD reactor was investigated by Wang et al.[12]. The authors used a high voltage (HV) electrode surrounded by a quartz tube (functioning as dielectric barrier), filled with catalyst pellets, and they reached 98% NH_3 conversion, but the lowest EC was 343 kJ/mol, hence much higher than in thermocatalytic cracking.

A lower EC can be obtained in 'warm' plasmas, e.g. pin-to-pin low-current arc, gliding arc, atmospheric pressure glow discharge, and microwave plasma. In this plasma type, the gas temperature can exceed a few 1000 K, while the electron temperature reaches up to several eV (= several 10,000 K). These two temperature regimes define the warm plasma categorization. The best EC of such warm plasmas was recorded by Fedirchyk et al. in a pin-to-pin low-current arc plasma, reaching a value of 146 kJ/mol[18]. This EC is still higher than obtained in thermocatalytic cracking, but it was achieved without the use of a catalyst, which could reduce the overall process cost.

However, the NH_3 conversion in this reactor was quite low, i.e., around 8 % at the best EC, and around 40 % at an EC of about 200 kJ/mol. We believe this may be attributed to a limited fraction of gas passing through the active region responsible for NH_3 cracking. To better understand the limitations found in the experiments, computational models can be very useful, as they can reveal the underlying physical and chemical mechanisms.

Up to now, the only models available in literature for plasma-based NH_3 cracking are zero-dimensional (0D) models,[19,20] including some plug-flow models that describe the axial spatial variation based on the evolution in time[21,22]. A recent work by Bayer et al[22] employed such a plug-

flow model to study a low temperature RF plasma jet, which experimentally gave an EC of 2400 kJ/mol. The authors concluded that cracking 1 mol of NH_3 due to electron impact dissociation will always have an EC higher than the lower heating value of the product, 1.5 moles of H_2 (362 kJ/mol)[23]. They noted that thermal chemistry combined with plasma processes might have better performance, which is consistent with the experimental studies discussed above. The lower heating value of H_2 is an absolute ceiling for acceptable EC, since otherwise it would cost more energy to make H_2 than we can retrieve from oxidizing it.

These 0D models, however, do not account for transport processes. Because the chemistry in warm NH_3 plasmas might be localized in space, multidimensional models are needed for a more complete description of warm plasma-based NH_3 cracking. Multi-dimensional models require computational fluid dynamics (CFD), which demonstrated great success in helping to understand the underlying mechanisms of gas conversion in plasma reactors[24–27]. However, such models have not yet been developed for NH_3 plasmas. Multi-dimensional modelling of an NH_3 flow (hence, not a plasma) was performed by Chein et al.[28], but they used only one chemical reaction on a catalyst surface to predict the conversion based on the local temperature. Chiuta et al.[29] simulated a microchannel catalytic reactor, solving for fluid flow and heat transfer, but they also used only one chemical reaction. In summary, while 0D models have been applied for simulating the detailed plasma chemistry[19–22] and CFD models for other (i.e., non-plasma) NH_3 cracking processes[28,29], there exist no models that combine realistic chemistry sets for warm plasmas with high-performance fully coupled multidimensional CFD simulations. Our paper will try to fill that gap.

We developed a model for the pin-to-pin low-current arc plasma reactor studied by Fedirchyk et. al.[18], which provided the best EC for plasma-based NH_3 cracking up to now in literature, but at somewhat limited conversion. Hence, our model should provide us insights into how to improve the conversion without increasing the EC. However, before we can do so, we first need to better understand the underlying mechanisms, like gas flow profile, temperature profile, chemical pathways, and transport processes (of species and energy), as well as the present limitations in the reactor design, to suggest possible improvements in future work. This model is, to the best of our knowledge, the first self-consistent multidimensional NH_3 warm plasma model.

2 Model characteristics

The pin-to-pin low-current arc plasma reactor[18] has a relatively simple design. The feed gas is initialized with a swirler to form a vortex flow. The gas then flows around a high-voltage pin electrode, which is separated from the other pin (ground) electrode by a gap of 3-5 cm. The plasma forms between these two conductors. Our model is a fully coupled 2D axisymmetric model for NH_3 cracking, which self-consistently solves the Navier-Stokes, heat transfer, Ohmic current continuity and chemical transport equations.

First, we calculate the fluid flow in a 3D geometry, containing the tangential inlets and the first part of the tube (see details in section 2.2 below and the left side of Figure 2). The velocities in this geometry are sampled over a cut plane, and this is the inlet condition of a second self-consistent 2D axisymmetric model. The 2D axisymmetric model can capture the effects of diffusion and spatial variation in temperature, two key space-dependent properties that drive the degree of

conversion. A fully coupled 3D model would have a prohibitive computational cost to mesh-converge. The simplification from 3D to 2D axisymmetric geometry incurs a loss of gradients along the angular direction ($\frac{df}{d\theta} = 0$ for all quantities f). We expect however that these gradients are negligible, due to the rotationally symmetric geometry and problem description. However, an angular component of the flow field can still be present, and this means that the swirl of the gas flow is captured both in the 3D flow model and the 2D fully coupled part of our model. The model is self-consistently solved, meaning that the primary heat source is conductivity-dependent Joule heating and that the enthalpic contributions of all reactions are taken into account for local cooling/heating of the gas, among other physics, as described by the equations in section 2.4 below. The flow profile influences the chemical profile by supplying untreated gas to the chemically active region (see below), and is influenced by a change in local density, which can be due to chemical reactions or gas heating. The gas is thus not necessarily in local chemical equilibrium. However, we assume that there is thermal, Saha and excitation equilibrium ($T_g = T_e = T_v$). These assumptions are necessary to calculate the conductivity based on the gas temperature, and to work with a reasonably reduced chemistry set[30,31]. The coupling of the electric currents with heat transfer is a clear novelty of our work, and we apply this workflow for the first time to an NH_3 plasma reactor.

2.1 Experimental setup and definition of performance parameters

We validate the model by comparing with the experimental results reported by Fedirchyk et al.[18] . The reactor setup is shown in Figure 1.

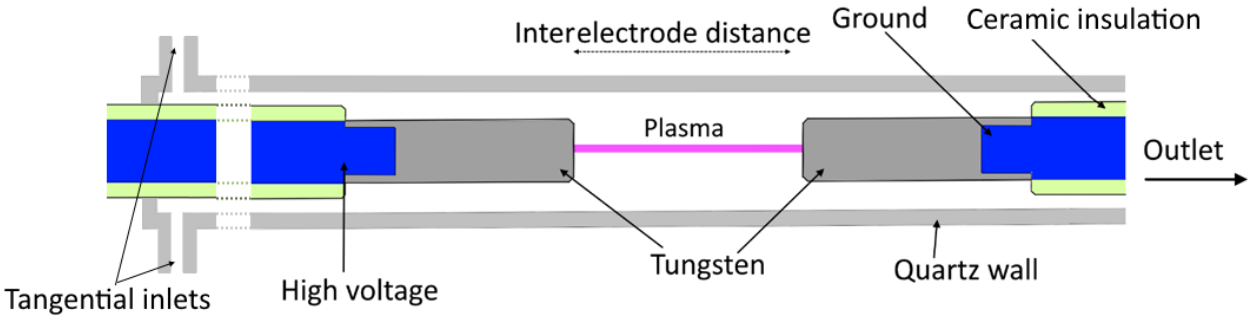

Figure 1. Schematic representation of the pin-to-pin reactor geometry used in Fedirchyk et al.[18]

The gas enters a quartz tube through four tangential inlets, which introduces a forward vortex flow into the reactor body. The amount of incoming gas is controlled by a Brooks SLA5850 mass flow controller. The gas is drawn from two NH_3 (≈99.96 %, Air Liquide) cylinders to maintain a steady gas flow rate (in the range of 5-20 NLM). A Technix SR12kV-10kW DC power supply delivers power values between 60-1200 W. The experimental power is determined by measuring the voltage drop and current with a Rohde & Schwarz RTB 2004 oscilloscope. The current is determined by measuring the voltage drop over a 10 Ω shunt resistor. The H_2 content in the output mixture is determined using a Rosemount™ X-Stream Enhanced general-purpose gas analyser

with a thermal conductivity detector (TCD). This H_2 fraction corresponds to a specific NH_3 fraction, which yields the unitless conversion (χ) with equation (2).

$$\chi = \frac{\dot{n}_{NH_3}^{in} - \dot{n}_{NH_3}^{out}}{\dot{n}_{NH_3}^{in}} \tag{2}$$

where $\dot{n}_{NH_3}^{in}$ and $\dot{n}_{NH_3}^{out}$ are the molar flow rates of NH_3 at the inlet and outlet, respectively (mol/s).

This definition is used directly in our model, while experimentally we have easier access to the total flow rate and the molar fractions. When calculating the conversion based on molar fractions, gas expansion has to be taken into account[18,32]. The experimentally determined conversion is then:

$$\chi = \frac{1 - y_{NH_3}^{out}}{1 + y_{NH_3}^{out}} \tag{3}$$

where $y_{NH_3}^{out}$ stands for the unitless molar fraction of NH_3 in a gas sample of the outlet effluent.

The reactor itself consists of a 50 cm long quartz tube with an inner radius of 8 mm and outer radius of 10 mm. In this tube, two stainless steel pin electrodes are inserted, covered by ceramic (6 mm radius), and with 3 cm long tungsten electrodes screwed on both ends, forming the powered and ground electrode. These pin electrodes are separated by a 3-5 cm discharge gap. This is the exact geometry under study in our work.

The key parameters that are directly compared between model and experiment are the specific energy input (SEI) per mole of NH_3, conversion (χ) and energy cost (EC). The SEI is the supplied energy in the reactor per mole of NH_3 in the feed (kJ/mol).

$$SEI = \frac{P}{\dot{n}_{NH_3}^{in}} \tag{4}$$

where P is the plasma power (W), and $\dot{n}_{NH_3}^{in}$ is defined above.

The EC (kJ/mol) is the amount of energy needed to convert one mol of NH_3 to H_2 gas.

$$EC = \frac{SEI}{\chi} \tag{5}$$

2.2 3D gas flow model

In the 3D model we solve the Reynolds-Averaged Navier-Stokes Shear Stress Transport (RANS SST) turbulence model[33–35]:

$$\rho(\vec{v} \cdot \vec{\nabla})\vec{v} = \vec{\nabla} \cdot [-p\boldsymbol{I} + (\mu + \mu_T)\left\{\vec{\nabla} \otimes \vec{v} + (\vec{\nabla} \otimes \vec{v})^{\mathrm{T}} - \frac{2}{3}\left(\vec{\nabla} \cdot \vec{v}\right)\mathbf{I}\right\} - \frac{2}{3}\rho k_T \mathbf{I}] \tag{6}$$

where ρ is the mass density of the gas mixture (kg/m^3), $\vec{v}$ is the velocity vector (m/s), p is the pressure (Pa), μ is the dynamic viscosity (Pa s), μ_T is the turbulent viscosity (Pa s), $\vec{\nabla} \otimes \vec{v}$ is the outer product of $\vec{\nabla}$ with the velocity vector, k_T is the turbulent kinetic energy (m^2/s^2), **I** is the 3x3 identity matrix and superscript T represents the transpose. This is a tensor-equation of rank 2, corresponding to nine differential equations. The equations are closed by including a differential equation for the turbulent kinetic energy k_T, and the specific dissipation rate ω:

$$\rho\left(\vec{v}\cdot\vec{\nabla}\right)k_T = \vec{\nabla}\left[(\mu + \mu_T\sigma_k)\vec{\nabla}k_T\right] + P - \beta_0^*\rho\omega k_T \tag{7}$$

$$\rho\left(\vec{v}\cdot\vec{\nabla}\right)\omega = \vec{\nabla}\left[(\mu + \mu_T\sigma_\omega)\vec{\nabla}\omega\right] + \frac{\gamma}{\mu_T}\rho P - \rho\beta\omega^2 + \frac{2(1-f_{v1})\sigma_{\omega 2}\rho}{\omega}\vec{\nabla}k_T\cdot\vec{\nabla}\omega \tag{8}$$

Where $\sigma_k, \beta_0^*, \gamma, \sigma_\omega, \sigma_{\omega 2}, \beta$ are turbulence parameters, f_{v1} is a blending function and P is the turbulent kinetic energy source term; for more details, see Menter et al[35].

The geometry of the swirler is shown in Figure 2. The first part of the reactor (described in the 3D model) is a cylinder with a length of 20 cm, consisting of two concentric tubes, i.e., the outer quartz wall (with inner radius of 8 mm; cf. section 2.1) and the ceramic tube surrounding the pin electrode (with outer radius of 6 mm), see also Figure 1 for details. Hence, the gap between both concentric cylinders is 2 mm. This aspect ratio of 100:1 reflects the substantial difference between its length (20 cm) and gap (2 mm). There are four symmetrical tangential inlets, spaced 90°, and we can leverage this to reduce the computational domain by a factor of four, by only simulating one inlet and adding a symmetry boundary condition to the boundary separating these quarters. Figure 2a presents the swirler geometry, as well as the simulated domain and the relevant symmetry profile. We use a tetrahedral mesh with boundary layers for the entire geometry, as this proved to yield better convergence than a partial tetrahedral and partially swept mesh. The final mesh has 3.4 million elements and is represented in Figure 2b for the first 5 mm of the geometry. The full computational domain of the 3D model is shown in Figure 2c. Note that this only represents the first 20 cm of the entire plasma reactor (which has a total length of 50 cm). The cut plane where the 3D gas velocities are converted to cylindrical coordinates for the inlet of the 2D axisymmetric model is schematically indicated by the vertical line, but its position varies for the different interelectrode distances investigated in this work. Specifically, it varies between 17 and 19 cm from the left boundary of the tube, where the actual gas inlets are located. The velocities are transformed from the 3D to the 2D axisymmetric coordinate system in the classical way[24,36], by equations (9)-(11)

$$v_r = \frac{xv_x + yv_y}{\sqrt{x^2+y^2}} \tag{9}$$

$$v_\theta = \frac{xv_y - yv_x}{\sqrt{x^2 + y^2}} \tag{10}$$

$$v_z = v_z \tag{11}$$

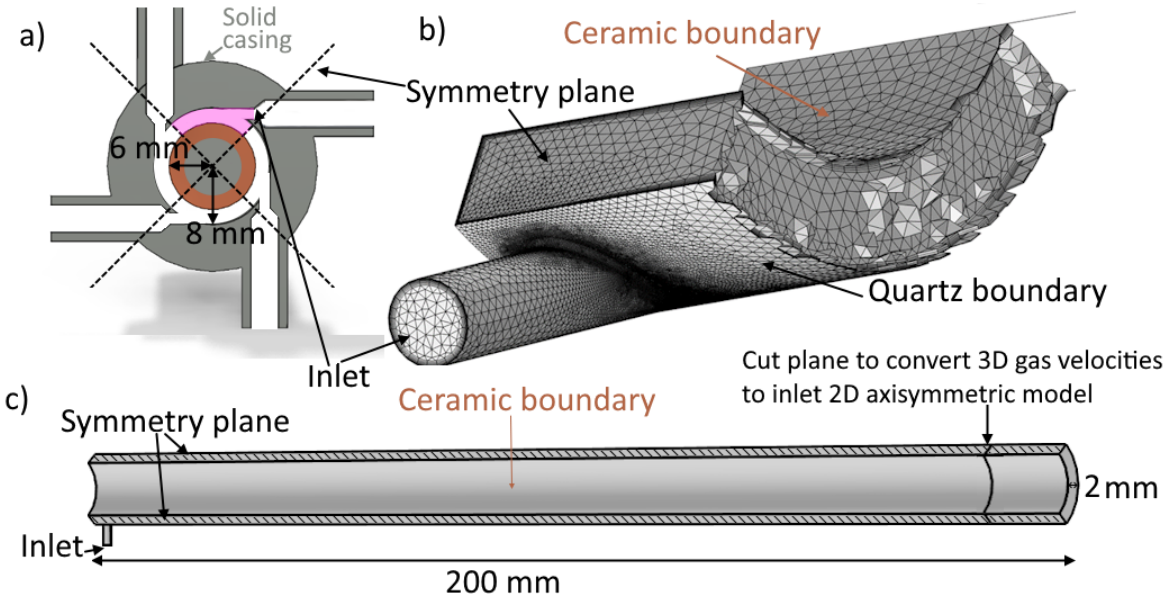

Figure 2. a) Front view of the real 3D geometry, with the inner and outer diameter of the gas region indicated: the central dark grey region is the electrode, the brown region is the ceramic surrounding the pin electrode, the white region is the actual gas domain, the pink region indicates the simulated (gas-phase) domain (only one quarter of the entire gas-phase domain), and the four-fold rotational symmetry is also indicated. b) Example of the mesh in the first 5 mm of the reactor. c) Side view of the entire gas phase domain as used in the 3D model, with dimensions and symmetry plane indicated. Note that it represents only the first 200 mm of the entire reactor (which has a total length of 500 mm).

2.3 Geometry and boundary conditions

Figure 3 presents the geometry of the pin-to-pin reactor, as used in the 2D axisymmetric model. The symmetry line at r = 0 mm allows us to reduce the geometry of the pin-to-pin reactor from 3D to 2D axisymmetric, significantly reducing the computational cost. This assumption is not exact, because in the experiment the plasma arc is not static but can move around. The plasma centre will therefore not always be aligned with the symmetry line. However, due to the flow profile, being more or less laminar in the region described by the 2D model, the plasma column can be approximated to remain fixed at the symmetry line.

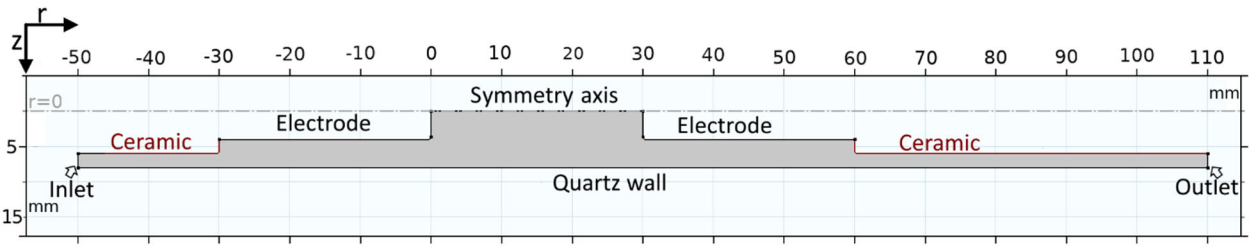

Figure 3. Geometry of the pin-to-pin 2D axisymmetric model, with all boundaries indicated. The interelectrode gap is 30 mm, as well as the length of both pin electrodes, and we include 20 mm length for the gas flowing around the protective ceramic for the powered electrode, and 50 mm for the ground. The radius of both electrodes is 4 mm, while the radius of the protective ceramics is 6 mm. The gas-phase region (where the gas flows, in between quartz tube and ceramic/electrodes) is indicated in grey.

A full overview of the boundary conditions is listed in the Supporting Information (SI), section S.1, Table S1 and Figure S1. The inflow conditions on the left boundary are determined by the calculated gas flow profile angularly averaged over a cut plane in the 3D gas flow model, as described in previous section 2.2. The experimental conditions consist of 100% NH_3, but this boundary condition would be computationally less stable, so a background concentration of 10^{-10} (mol/mol) molar fraction is used for all species in the model besides NH_3.

The electrode tips (at 0 and 30 mm) are thermally insulated; this is necessary because we cannot resolve the plasma sheath close to these electrodes. The plasma sheath violates the assumption of $T_e = T_g$ and the electron density is not equal to its equilibrium value. The fact that we cannot resolve the electrode sheaths has no significant impact on the plasma column properties, as demonstrated by previous modelling work from our group[37].

The terminal electrical boundary condition on the powered electrode tip (at 0 mm) allows us to make the simulation current-controlled, as is the case for the experimental setup. We can specify the total current, while the voltage needed to supply this current is then self-consistently calculated[38].

The quartz tube has two energy loss terms, i.e., natural external convection for a cylinder of radius 10 mm (i.e., the outer radius of the quartz tube), and surface-to-ambient radiation with an emissivity of 0.75[39], which is a representative value for quartz. At the outlet we assume that there is no conductive transport of heat (only convective). The flow boundary condition is based on pressure, to not influence the flow field near the outlet.

2.4 2D axisymmetric fully coupled model: governing equations

The fully coupled 2D axisymmetric model solves the heat balance equation, Ohmic current continuity, laminar flow approximation of the Navier-Stokes equation, and mass balance equations of all species. Since the model is 2D axisymmetric, there are no gradients in the θ component.

The model is similar to the work presented by Maerivoet et al[24]; however, we developed this model for an NH_3 plasma, while the previous study was on dry reforming of CH_4. In addition, the main improvement is the self-consistently calculated heat source shape, which is based on the electrical conductivity calculated from an equilibrium assumption. This closes the set of equations and eliminates fitting the model to a single experimental result. The only setup-dependent experimental

parameters that are used in this model are the flow rate, electrical current and reactor geometry, all explicitly controlled by the experimentalist. Some experimental or more fundamental modelling input is still required in the form of rate coefficients of specific reactions and properties of individual species.

The main assumptions of the model are that the chemistry is predominantly thermal, the mechanism of cathode emission does not significantly influence the properties of the main plasma column, and the flow is sufficiently laminar so that turbulent mixing effects can be neglected. The first assumption is validated by recent work on detailed chemical kinetics modelling, including thermal and non-thermal (i.e., electron-induced, excited state and ion) chemistry, applied to a wide range of conditions, where we demonstrate that the chemistry is indeed predominantly thermal in warm plasmas[40]. Therefore, we will omit all electron impact kinetics and ion chemistry from our chemical sets and the 2D model. Moreover, we will also validate this assumption later in our paper. The second assumption was validated by previous modelling work by Tsonev et al.[37] The third assumption is justified because the turbulent intensity is never more than 10^{-5}, as will be shown in section 3.1 below.

(a) Ohmic current continuity equations

The current is governed by the Ohmic current continuity equations, equations (12)-(14)[38].

$$\vec{E} = -\vec{\nabla}V \tag{12}$$

$$\vec{\nabla} \cdot \vec{J} = 0 \tag{13}$$

$$\vec{J} = \sigma\vec{E} \tag{14}$$

Equation (12) is valid in the electrostatics case, where no significant magnetic fields are present. In our model, we assume that the self-induced magnetic field is negligible. Equation (13) states that current is conserved and there is no time-dependent build-up of charge. Finally, equation (14) is Ohm's microscopic law. The current is directly proportional to the local electric field. In its most general form, this is a tensor-equation, however σ is assumed to be isotropic and is given by Liebermann's cold dc plasma conductivity[30] (equation (15)). A lower bound for the conductivity is employed to improve numerical convergence. This lower bound is fixed at 10^{-8} S/m. It is low enough that almost no (<0.1%) current flows through regions with minimal conductivity.

$$\sigma = \frac{e^2 n_e}{m_e \nu_m} \tag{15}$$

ν_m is the electron collision frequency (Hz), e the elementary charge (C), m_e the electron mass (kg), and n_e the electron density (m^{-3}). The electron collision frequency is the sum over the individual collision frequencies of all neutral species. The electron collision frequency is calculated for each neutral species as an integral over the electron cross-sections of the LXCat database[41–46] (equation (16)).

$$\nu_m = \sqrt{2/m_e} \sum_j N_j \int_0^\infty f(E)\sigma_{j,e}(E)EdE \tag{16}$$

N_j is the density of neutral species j at equilibrium (m^{-3}), f ($J^{-3/2}$) is the electron energy distribution function (EEDF), which is assumed to be a Maxwellian for the electron temperature equal to the gas temperature. $\sigma_{j,e}$ is the electron neutral momentum transfer cross-section (m^2) and E is the electron energy (J).

The electron density n_e is calculated from the temperature-dependent equilibrium ionization of the gas. The ionization degree is calculated by minimizing the Gibbs free energy, which comes from the NASA 9 polynomials[47]. CANTERA[48] is employed for this minimization. The assumption that the electron temperature is equal to the gas temperature is not strictly valid. Indeed, as noted earlier, close to the electrodes this assumption clearly does not hold. Even in the main plasma column, the electron temperature is likely higher than the gas temperature. This affects the calculated electrical conductivity, which will affect the heat source shape. However, in section S.7. of the SI we discuss the effect of the heat source shape, and we show that it has no effect on the conversion EC in the plasma.

However, the electron chemistry can also affect the gas composition. Unfortunately, it is currently computationally unfeasible to properly resolve the electron behaviour in a multidimensional fully coupled model as presented in this work. Nevertheless, we believe the multidimensional model has much added value, as it provides valuable information on the gradients in the temperature and species densities, which is more important to understand the process than what we gain from a 0D model, which includes an accurate description of the role of electrons in our chemistry. It would be even better to develop a multidimensional model that accounts for all electron-induced processes, and this should be targeted in the future, as soon as this becomes computationally feasible.

The species present in this thermodynamic equilibrium model are e^-, H, H^+, H_2, H_2^+, N, N^+, N_2, N_2^+, N_3, NH, NH^+, NH_2, NH_3, NH_4^+, N_2H_2, and N_2H_4. These are all the dominant neutral and positive ion species. Their molar fractions and the conductivity as a function of gas temperature are presented in SI, section S.2 (Figures S2 and S3).

This method of calculating the conductivity has a solid theoretical foundation, although it is based on certain assumptions to keep the model feasible to solve. The electron density is likely somewhat underestimated, since we assume local thermodynamic equilibrium and thus, there is no electron impact ionization, or any other ionization reactions, that can increase the electron density. Furthermore, the EEDF is assumed to be Maxwellian. If the true EEDF has a different shape, this would impact the collision frequency. The degree of non-equilibrium depends on the gas temperature and local electric fields. Due to the high temperatures (> 4000 K) in the arc, the electron temperature will be relatively close to the gas temperature as ionization of the gas can proceed via associative ionization. As such we estimate the electron temperature to never exceed 2 eV. The assumption of a Maxwellian EEDF is valid under conditions of high collision frequency,

so that the energy of the electrons can efficiently be redistributed. This is usually the case for plasmas with currents above 50 mA[49], and based on our experience, this assumption is also reasonable at somewhat lower currents, however, for currents below ~25mA the model overestimates the EC, this indicates that non-thermal chemical processes, like electron induced dissociation of hydrogen can be important in this regime. Overall, these assumptions can capture the main trends of the plasma behaviour, as will be demonstrated in section 3.2 below.

(b) Heat transfer equation

Heat transfer is governed by equation (17)[50,51].

$$\rho C_p \vec{v} \cdot \vec{\nabla} T + \vec{\nabla} \cdot \vec{q} + \sum_{n}^{N_{react}} H_n R_n = \vec{E} \cdot \vec{J} \tag{17}$$

ρ is the mass density (kg/m^3), C_p is the heat capacity at constant pressure (J/(kg K)), $\vec{v}$ is the velocity vector (m/s), T is the absolute temperature (K), $\vec{q}$ is the heat flux vector (W/m^2), H_n is the enthalpy of reaction n (J/mol), R_n is the reaction rate of reaction n (mol/(m^3 s)), $\vec{E}$ is the local electric field (V/m) and $\vec{J}$ is the current density (A/m^2). This equation is clearly dependent on the Ohmic current equation ($\vec{E}, \vec{J}$), the Navier-Stokes equation ($\rho, \vec{v}$) and chemistry (H_n, R_n). The heat sources are the Joule heating and the enthalpy of chemical reactions. The heat diffusive flux vector (often called conductive flux) is calculated as: $\vec{q} = -k\vec{\nabla}T$, where k is the isotropic heat conductivity of the mixture, which is the average of the arithmetic and harmonic weighted means of the individual species[52].

(c) Fluid flow equations

The governing equations for fluid flow are a laminar formulation of the Navier-Stokes equation (Equation (18)-(19)) [33,34].

$$\rho(\vec{v} \cdot \vec{\nabla})\vec{v} = \vec{\nabla} \cdot [-p\boldsymbol{I} + \mu(\vec{\nabla} \otimes \vec{v}) + \mu(\vec{\nabla} \otimes \vec{v})^T - \frac{2}{3}\mu(\vec{\nabla} \cdot \vec{v})\mathbf{I}] \tag{18}$$

$$\vec{\nabla}(\rho\vec{v}) = 0 \tag{19}$$

While this 2D axisymmetric model contains no gradient in the angular component, equations 18 and 19 are solved in all three cylindrical dimensions.

Equation (19) represents the conservation of mass. We opt to solve with a laminar approximation since the turbulent intensity at the inlet of the 2D model is of the order of 10^{-6}. (see section 3.1 for the calculation). Since increasing the temperature increases the viscosity and decreases the density more than it increases the flow velocity, the Reynolds number will drop with increasing temperature, making the flow even more laminar. To test this assumption, we performed one simulation using the SST model, and this gave a maximum turbulent kinetic energy of only 0.15 m^2/s^2, which is a negligible amount of energy, hence fully justifying our assumption of laminar flow.

The viscosity is calculated by kinetic theory as outlined by Wilke et al[50,53]. In section S.3. in the SI we show that there is a negligible difference between our gas viscosity and more complicated plasma viscosity calculations. Due to the low ionization degree of the plasma in the modelled temperature ranges and the assumption that the electron temperature does not lead to significant deviations in the composition of the gas, we believe that the assumption to calculate the viscosity of the gas from the neutral components is valid, as was reported previously in literature[49,54,55].

(d) Transport of species equations

The transport of species is governed by equation (20), which is solved for each species in the model.

$$\vec{\nabla} \cdot \vec{J_i} + \rho \vec{v} \cdot \vec{\nabla} \omega_i = R_i \tag{20}$$

$\vec{J_i}$ is the diffusive flux vector of species i (kg/(m^{2}s)), ω_i is the species mass fraction (kg/kg) and R_i is the net production rate of species i (kg/(m^{3}s). The diffusive flux vector $\vec{J_i}$ is calculated by equation (21).

$$\vec{J_i} = -(\rho D_i^m \vec{\nabla} \omega_i + \rho \omega_i D_i^m \frac{\vec{\nabla} M_n}{M_n} - \overrightarrow{J_{c,i}}) \tag{21}$$

where D_i^m is the mixture-average diffusion coefficient (m^2/s), M_n the mean mixture molar mass (kg/mol) and $\overrightarrow{J_{c,i}}$ the multi-component diffusive flux correction term (kg/s). The first two terms are gradient-driven diffusive terms, while the last term ensures that the net diffusive mass flux is zero[50,51].

This set of equations is fully coupled. Indeed, as mentioned above, the heat source is defined by the enthalpic contributions of the chemical reactions and Joule heating from the applied current. The conductivity is a function of temperature and is thus influenced by how the heat produced from the Joule heating is distributed. The velocity profile is a function of the chemical composition and of the temperature, via the density and viscosity. Furthermore, the chemical composition itself is directly influenced by the velocity, due to the convective transport term. The rate of all reactions is strongly dependent on the temperature, completing the loop of dependencies. As all equations depend on each other, we used a fully coupled solver, namely COMSOL®'s Automatic (Newton) scheme with its direct PARDISO solver[56].

2.5 Chemistry

Previous NH_3 plasma models, for low-temperature conditions, ranging from 300 K up to 1000 K, show that NH_3 cracking is heavily dependent on the gas temperature, which is a first indication of the importance of thermal kinetics[19]. As the gas temperature in warm plasma reactors, like the pin-to-pin reactor studied here, is on the order of 4000 K[18,57] and the electron temperature remains below 2 eV, thermal kinetics of NH_3 will indeed be the driving factor for NH_3 conversion in warm

plasma[40]. This is why no electron impact reactions or ion chemistry are included in the 2D axisymmetric model. Furthermore, multiple shock-tube experiments and kinetic model studies by Alturaifi et al.[58] and by Glarborg et al.[59] show that the decomposition of NH_3 via thermal kinetics above 3000 K happens on a sub-millisecond timescale. While both papers build a well-fitting thermal NH_3 set, it is only validated by experiments for low NH_3 fractions, i.e., 0.4–1 %, diluted in Ar. We constructed a thermal NH_3 set, based on the shock-tube and modelling results, with the goal of modelling warm plasmas in undiluted NH_3.

Our full thermal reaction set consists of 13 species and 50 reactions and can be found in Table S2 of the SI, section S.4. This is a general reaction set for NH_3 cracking in the temperature range of 300 to 6000 K, applicable for multiple types of reactors and processes. Unfortunately, multidimensional simulations with such a complex chemistry set are computationally still unfeasible. Therefore, we reduced the full thermal NH_3 set, using a sensitivity analysis in a 0D model, similar to the reduction performed for the kinetics of Maerivoet et al[24], for our pin-to-pin warm plasma model. The details are described in SI, section S.5 (Figure S5), and the comparison of the species molar concentrations between the full and reduced sets is presented in Figures S5-S6.

The set of species included in our 2D model can be found in Table 1, while the reactions considered in the reduced thermal chemistry set are listed in Table S3 of the SI, section S.4.

Table 1 - List of species used in the 2D model.

H	NH	trans-N_2H_2 (t-N_2H_2)
H_2	NH_2	cis-N_2H_2 (c-N_2H_2)
N	NH_3	H_2NN
N_2		N_2H_3
		N_2H_4

3 Results and discussion

First, we present the gas flow profile from the 3D CFD model, and then we compare our calculated electrical characteristics and NH_3 conversion and EC with experimental results, for model validation. Subsequently, we discuss in detail the chemical, thermal and flow properties of the plasma reactor. Finally, we analyse the distribution of energy and identify the driving chemical processes.

3.1 Calculated 3D gas flow profile

A typical calculated 3D gas flow profile is presented in Figure 4, for 20 NLM. The flow velocity reaches 67 m/s at the inlets, but drops significantly while the gas flows through the reactor, to values of around 6 m/s. The turbulent kinetic energy reaches a maximum of 50 m^2/s^2 at the tangential inlets, and it decays rapidly over the length of the tube, until it reaches a negligible

average value of 10^{-9} m^2/s^2 at 19 cm, while the turbulent intensity reaches a value of 4.1×10^{-6}. The turbulent intensity is defined by equation (22)[60].

$$I_{turb} = \sqrt{\frac{3k_T}{2v_{ref}^2}} \tag{22}$$

Where k is the turbulent kinetic energy and v_{ref} is the reference velocity, which is the volume flow divided by the cross-sectional area.

This very low turbulent kinetic energy justifies the use of a laminar approximation for the 2D axisymmetric model (see section 2.4 above).

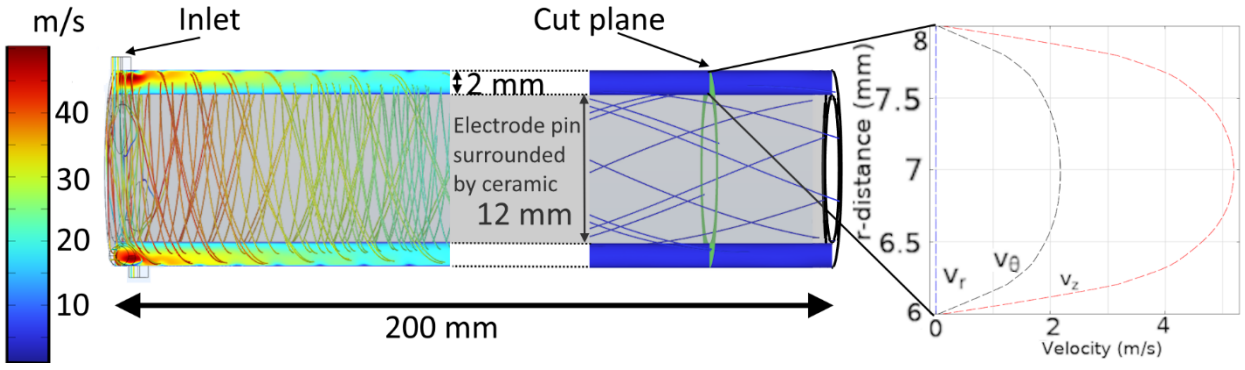

Figure 4. Flow profile for an inlet flow rate of 20 NLM and 25 cm between gas inlet and electrode tip (hence the latter is not shown in this figure, as the pin extends beyond the region of this figure). The pin electrode surrounded by ceramic is indicated by the semi-transparent, grey-shaded area, so the gas flow swirls around it. The velocity is indicated in m/s. The inlet and cut plane are also indicated, as well as all relevant dimensions. The radial, tangential and axial components of the extracted velocity profile at the cut plane are shown at the right-hand side of the figure.

The right-hand side of Figure 4 illustrates a typical flow profile as it is imported to the 2D axisymmetric model: the radial velocity is always very small, the tangential (θ) component decays from a maximum of 55 m/s to about 2 m/s at the cut plane, while the flow moves away from the swirl inlets. The z-component is constant at about 5 m/s over the length of the tube, since the gas does not significantly expand before coming in contact with the plasma, so the axial velocity must be constant to maintain conservation of total flow. Close to the inlets, the tangential component dominates, but closer to the plasma, only the axial component remains.

3.2 Model validation with experimental data

We validated our model over a wide range of applied experimental currents (2 - 180 mA) and flow rates (5 - 20 NLM), which corresponds to an SEI range of 7.1 – 54.8 kJ/mol. First, we compare the current-power characteristics with experimental results, followed by a comparison of the more general performance characteristics, i.e., NH_3 conversion and corresponding EC.

3.2.1 Current-power characteristics

Figure 5 illustrates the calculated power as a function of applied current, between 2 and 180 mA, compared with the experimental data of Fedirchyk et al[18]. Both the experimental and calculated power-current characteristics follow the empirical law $P = rI^{2-b}$, where r and b are parameters > 0. This law is based on the fact that the plasma resistivity decreases following a power law as a function of the applied current[61]. For the experimental results, we find the relationship P=3183 $I^{0.86}$, while the simulation yields P= 758 $I^{0.36}$, where the current is in Amperes and the power in Watts.

While the general empirical function holds for both the experiment and simulation, albeit with different parameter values, the power values corresponding to a particular current can be quite far off. However, the absolute values of calculated power are in the correct order of magnitude. The latter is also not straightforward, because no fitting parameters are used in the model, which is often the case in literature, to match with the experiments. Our comparison allows us to really judge the predictive capabilities of the model. It indicates that the assumptions underlying the plasma conductivity might be too strict for the system under study. Since the main goal of the power calculation from the electrical current is to provide plasma heating, we will thus focus on the comparison between calculated and experimental SEI values. Even if the latter corresponds to different currents, using the SEI as variable allows us to obtain valuable information about the plasma characteristics at realistic experimental conditions.

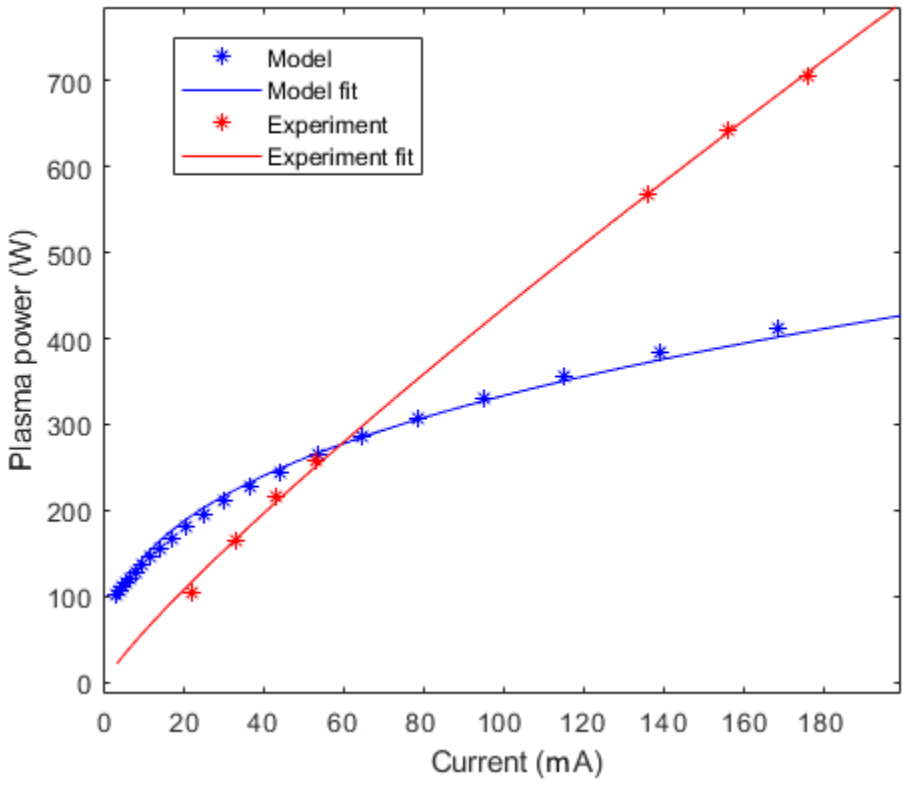

Figure 5. Calculated (blue) and experimental (red) plasma power as a function of current, for an interelectrode distance of 3 cm, and gas flow rate of 20 NLM. Solid lines indicate the power law fit[62].

3.2.2 Reactor performance as a function of SEI

Figure 6 illustrates the calculated conversion and EC as a function of SEI, in comparison with the experimental data, for three different flow rates, showing quite good agreement. The conversion clearly rises with SEI, which is logical, because NH_3 cracking is an endothermic reaction, and more power is deposited to the same amount of feed gas.

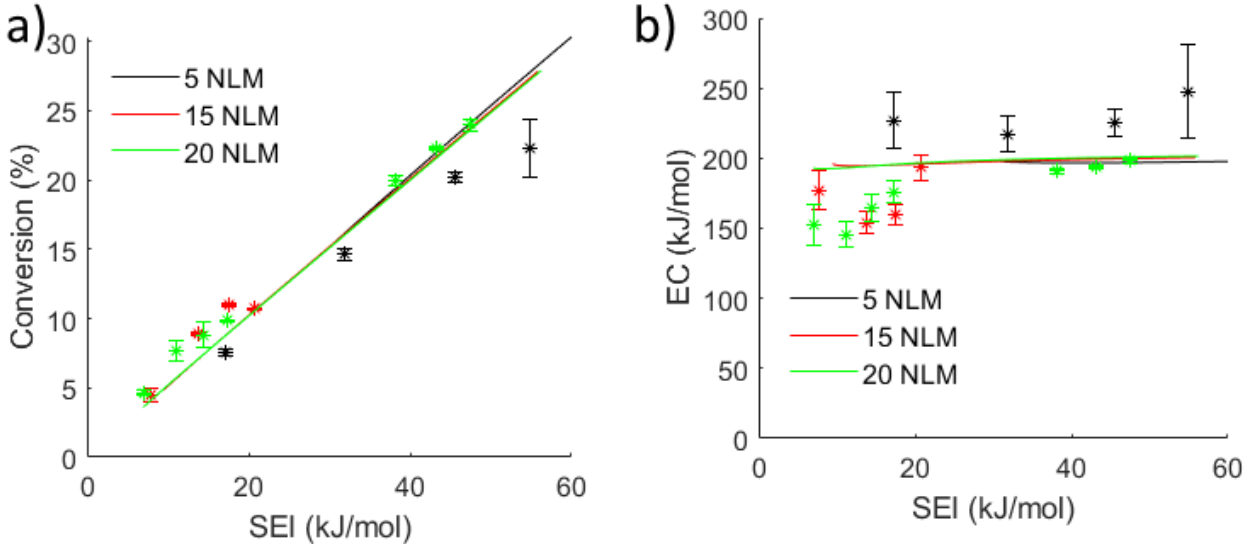

Figure 6. a) Conversion, and b) EC vs SEI, for three different flow rates (see legend), comparing model (solid lines) with experiment (symbols). Interelectrode distance of 3 cm.

The model shows an interesting trend that is confirmed by the experiments: the NH_3 conversion in our pin-to-pin arc reactor is strongly dependent on the SEI but is almost independent of the flow rate. Furthermore, the EC of cracking remains remarkably stable over the SEI range under investigation. The constant EC in Figure 6b is a result of the proportionally constant energy losses, as discussed later. Indeed, we will show that a constant fraction of the deposited energy is used for endothermic NH_3 cracking. In the experimental results, we do observe a somewhat elevated EC at 5 NLM over the entire SEI range (black symbols), but also a minimum in the EC at low SEI, for 15 and 20 NLM, while our model predicts a constant EC. This discrepancy at very low flow rates (5 NLM) can be explained because in the experiments, the plasma deviates from the perfect axisymmetric geometry assumed by the 2D model. Indeed, at low flow rates, e.g., 5 NLM, the plasma is less constricted by the gas flow cooling, which can result in an offset in location of the experimental plasma centre with respect to the centre of the reactor. This (small) difference in plasma location between experiments and model may affect the fraction of gas passing through the region where conversion happens, and this may explain the somewhat higher conversion and lower EC in the model. On the other hand, at low current (and thus low SEI), plasma instabilities and plasma chemical effects, not yet included in this model, could affect the conversion, explaining the discrepancy between model and experiment at low SEI. Overall, we believe the agreement is

reasonable, also in absolute values, certainly keeping in mind that not any experimental fitting parameter is used, and everything is calculated self-consistently

The fact that the conversion rises (more or less) linearly with SEI, and the EC stays more or less constant, indicates that the reactor performance can be enhanced by increasing the SEI: although this may slightly increase the EC (see experimental data points), the substantially higher conversion largely compensates for this. We therefore believe that increasing the SEI, up to 220 kJ/mol will eventually yield full conversion, while keeping a close to constant EC. However, we would need additional experimental data at much higher SEIs to solidify this claim.

3.3 Gaining insight in plasma-based NH_3 cracking

In this section we discuss the underlying physics and chemistry of the plasma reactor. We first analyse the velocity, temperature and NH_3 mass fraction profile, and correspondingly the chemically active region. Secondly, we discuss which reactions drive the conversion and how this influences the flow of energy in the reactor volume. Finally, we discuss the NH_3 transport to the chemically active region.

3.3.1 Velocity, temperature and NH3 mass fraction profiles, and chemically active region

Figure 7 illustrates the gas flow profile, temperature profile, NH_3 mass fraction profile and chemically active region as calculated by our model, for a flow rate of 15 NLM and SEI of 29 kJ/mol.

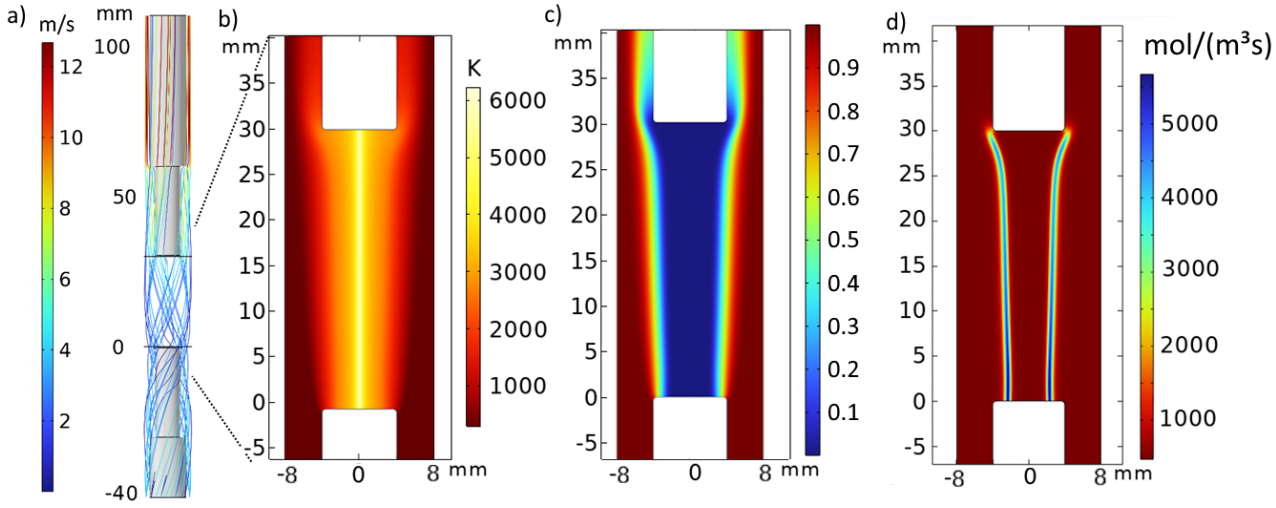

Figure 7. Calculated gas velocity profile (a), temperature profile (b), NH_3 mass fraction (c), and rate of NH_3 destruction (d), at a flow rate of 15 NLM and SEI of 29 kJ/mol.

The gas flow (Figure 7a) significantly speeds up from 4 m/s near the tip of the powered (bottom) electrode, to 12 m/s when reaching the base of the grounded (upper) electrode, due to gas expansion in the plasma from NH_3 dissociation and elevated temperatures, and the swirling flow (present around the bottom electrode pin) has nearly disappeared, followed by a laminar flow in

the region between both pin electrodes. Figure 7a is constructed by rotating the results from our 2D simulation around the central axis, giving a 3D plot.

Figure 7b shows that our model predicts a maximum temperature in the central plasma column of about 6000 K, while the gas close to the reactor walls remains at room temperature. This is because the deposition of energy is very close to the central axis. Indeed, more than 95% of the power is deposited within 0.3 mm of the symmetry axis (see section 3.5 below).

Figure 7c shows that NH_3 is fully converted in the high temperature zone (T > 3000 K), while its mass fraction is above 50% if the temperature drops below 1400 K. From 30 mm onwards (i.e., the start of the grounded (upper) pin electrode), the treated and untreated gas mixes without converting further, eventually forming a homogenous mixture of NH_3, H_2 and N_2 at the reactor outlet.

Finally, Figure 7d identifies the so-called "chemically active zone", by plotting the rate of destruction of NH_3. This is the sum over all reactions destroying/producing NH_3. In this zone the NH_3 destruction rate is at least 500 mol/(m³ s) and reaches maximum values of 5000 mol/(m³ s). This corresponds to a temperature region between 2400 and 3000 K. A second important feature is that the local rate of destruction is nowhere negative in the entire reactor. This clearly shows that backreactions (formation of NH_3) are not present in this reactor. This is to be expected due to the very slow kinetics at low temperatures and the thermodynamic instability of NH_3 at elevated temperature. Note that higher temperatures (in the plasma core) also lead to full NH_3 decomposition (and this would be even faster), but the NH_3 gas simply does not reach this hot plasma core, as it arrives in the interelectrode region from the sides (surrounding the electrode pins) and is already fully converted in the chemically active region surrounding the hot plasma core, this is discussed in further detail in section 3.5.1. In this high temperature zone, the dominant thermal chemical reaction is H_2 splitting, as will be discussed in section 3.5.2.

3.3.2 Chemical pathway analysis

As shown in Figure 7 above, NH_3 decomposition occurs in a small temperature region (2400 - 3000 K) in the plasma. To understand which reactions are important at different locations in the reactor, a detailed pathway analysis is needed. Figure 8 illustrates the pathway analysis for 5 NLM and 25 mA (SEI = 58 kJ/mol). The picture is similar for the conditions of Figure 7 (15 NLM and SEI = 29 kJ/mol), but the lower flow rate of 5 NLM allows us to more easily compare with higher SEI, which is presented in the SI, section S.6. The most important net reaction rates are shown. As mentioned in SI, section S.4, all reactions are balanced, hence the arrows show the net conversion of one species to the other. For the intermediate species (NH_2, NH, trans-N_2H_2, cis-N_2H_2), the branching ratios of the most important reactions (also to other species) are depicted next to the reaction arrows. Contributions < 1 % are left out, for clarity. Any reaction denoting (+ M) requires a neutral third body as collisional partner to proceed.

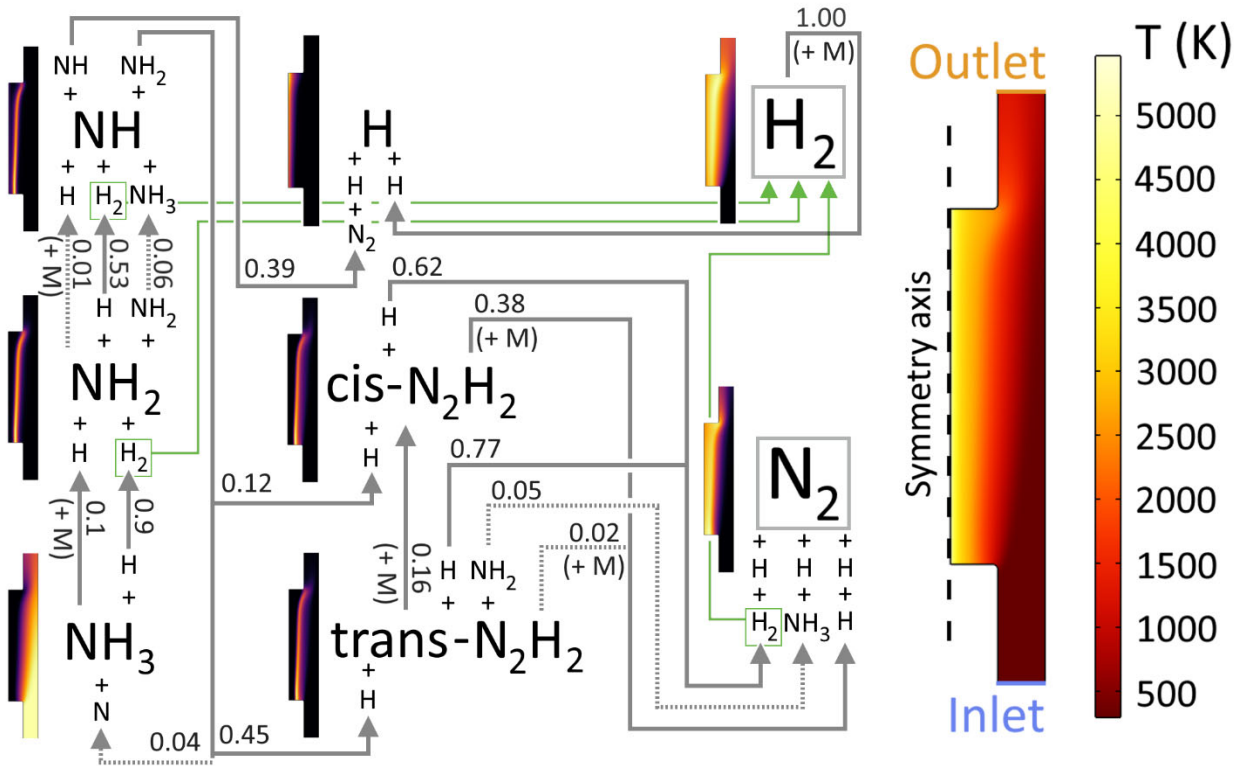

Figure 8. Reaction pathway analysis of NH_3 decomposition at 5 NLM, SEI = 58 kJ/mol. The 2D plots illustrate the mole fractions of the species, while the temperature profile is shown on the right. The arrow directions correspond to the net rates of the reactions in the complete reactor. The branching ratios for the destruction of a species are denoted next to the arrows, (+ M) is shown if the reaction requires a third body as neutral collision partner to proceed. Reactions contributing to less than 10 % of the species destruction are indicated with a dashed arrow, while reactions contributing less than 1 % are omitted, for clarity. Importantly, all produced (green) H_2 molecules are linked to the final H_2 product with green arrows.

The general trend of NH_3 decomposition is clearly shown in Figure 8: NH_3 decomposes into NH_2, followed by NH, after which the pathway branches, as detailed below. Taking a more detailed look, NH_3 is broken down to NH_2 via two reactions: while the reaction with H accounts for 90 % of the NH_3 destruction (and leads to H_2 formation), it is not possible without the reaction of NH_3 with M, as this reaction creates the first necessary H atoms. Therefore, the reaction of NH_3 with M is important to initiate the NH_3 decomposition.

Like NH_3, the decomposition of NH_2 to NH mainly occurs via reaction with an H atom (contribution of 53% and leading to H_2 formation). Furthermore, the NH_2 radical can also react with itself to form NH and NH_3 or it can decompose into NH upon collision with M (although both reactions are of minor importance), and in addition NH_2 reacts with NH to form both N_2H_2 isomers (as well as new H atoms) or to form NH_3 and N. Because not all NH_2 reacts to NH, the sum of the branching ratios for NH_2 destruction to NH is not equal to one. If we include the reaction of NH and NH_2 to cis- and trans-N_2H_2 and the reaction of NH_2 with trans-N_2H_2 into N_2, NH_3 and H, the sum of the branching ratios is equal to one.

From NH onwards, several pathways are possible. First, the reaction of NH with itself gives rise to the formation of N_2 and two H atoms (contribution of 39 %). In addition, NH reacts with NH_2, forming either trans-N_2H_2, cis-N_2H_2 or NH_3, as just mentioned above. The first two pathways are much more significant, accounting for 45 % and 12 % of NH destruction, respectively. While trans- and cis-N_2H_2 follow similar reaction pathways both for production and destruction, the major difference between these species is their enthalpy. Indeed, cis- and trans-N_2H_2 have an enthalpy of formation of 212 vs 200 kJ/mol at 300 K, and 392 vs 380 kJ/mol at 2800 K. As such, starting from trans-N_2H_2, three reactions lead to N_2 formation, with the reaction of H as co-reactant being the most important (and again producing H_2). However, 16 % of trans-N_2H_2 is converted via isomerization to cis-N_2H_2, after which cis-N_2H_2 reacts with H or with M into N_2 and H/H_2. Therefore, while cis-N_2H_2 is an important intermediate from NH to N_2, it is also important in the trans-N_2H_2 destruction pathway.

It is important to note that the most important reactions from NH_3 to NH_2 and NH create H_2 as the co-product, while using H as co-reactant. In addition, both major cis- and trans-N_2H_2 decomposition pathways to N_2 (upon reaction with H) also create H_2. Therefore, all these produced H_2 molecules are also highlighted in green in Figure 8, as they are the major reaction product, and they are linked to the final H_2 product with green arrows. Figure 8 also shows an arrow for the decomposition of H_2 towards H, which is dominant over H atom recombination into H_2 (see also section 3.5.2 below).

In the SI, Section S.6, Figure S8 shows a similar pathway analysis, but for 5 NLM and 1.25 A, hence much higher power and SEI (231 kJ/mol). The general NH_3 decomposition, via NH_2, NH, cis- or trans-N_2H_2 and eventually towards N_2 and H_2, looks very similar to Figure 8. However, the amount of NH_3 reaching the end of the plasma reactor is significantly lower, which is expected, due to the higher conversion at higher SEI. The higher SEI means 40% more H_2 is dissociated to H atoms, and these H atoms diffuse very fast and shift the dominant NH_3 destruction mechanism even more to reactions with H (instead of M), thus producing more H_2 as well.

The different intermediate species occur in different temperature ranges: both cis- and trans- N_2H_2 are formed between 2150 and 2600 K, and they are destroyed between 2600 K and 2900 K, while NH_2 is mainly formed between 2200 and 2700 K, NH is formed between 2500 and 2800 K, and the H atoms mainly reside in the plasma core at temperatures above 2700 K. All these reactions happen in a relatively narrow zone between 2 and 3.5 mm from the symmetry axis. Therefore, we call this zone with a temperature between 2400 and 3000 K the chemically active region, where most of the NH_3 is destroyed and most of the products are formed. The high plasma temperature in the central column plays a significant role in providing the crucial H atoms to this zone and it is thus not necessarily detrimental that the temperature is higher here than strictly needed. Indeed, as higher temperatures give rise to more H atoms (see the thermodynamic equilibrium distribution in Figure S2 in SI), more H atoms can diffuse towards the chemically active region, further contributing to efficient NH_3 conversion. Furthermore, as we did not include charged species in our modelling and the plasma centre is the current-carrying region within the reactor, we cannot draw firm conclusions about the plasma core chemistry. While we see that H radicals are produced in the plasma core and diffuse outward, electron impact chemistry will likely create more H

radicals from H_2 splitting. This process might influence the NH_3 conversion chemistry in the chemically active zone by increasing the outward flux of H radicals.

Validation of chemical species pathways is difficult, but very important as most of the time only the resulting composition of the plasma is known. Spatial imaging of plasmas is therefore an important tool, which can be used by multidimensional plasma modellers to validate or disprove their model.

3.3.3 NH_3 transport

It is clear from the previous section that the chemistry is very localized, and thus, transport of NH_3 to the chemically active region is crucial. Transport of species (including NH_3) is determined by several characteristic timescales and corresponding dimensionless numbers. The Péclet number is the ratio of the diffusive timescale to the convective timescale, while the Damköhler number is the ratio of the convective timescale to the reactive timescale[63]. Instead of calculating these dimensionless numbers, we represent the respective timescales directly; see Table 2. The diffusive timescale is defined as the square of the characteristic length over the diffusion coefficient. The characteristic length is the radius of the tube (8 mm) for radial diffusion, and the interelectrode distance (3 cm) for axial diffusion. The convective timescale, or gas residence time, is the characteristic length over the radial/axial velocity, and finally the reaction timescale is given by the inlet concentration of NH_3 over the integrated reaction rate of all NH_3 destruction processes. Table 2 does not only list these definitions, but also typical values halfway between both electrodes.

Table 2. Definition and representative values (halfway between both electrodes), for comparing timescales in our pin-to-pin reactor, at 29 kJ/mol and 15 NLM. R is the tube radius, L is the interelectrode distance and $c_{NH_3}^{inlet}$ is the inlet concentration of NH_3.

	Radial diffusive timescale	Axial diffusive timescale	Radial convective timescale	Axial convective timescale	Reaction timescale
Definition	$\frac{R^2}{D_{NH_3}}$	$\frac{L^2}{D_{NH_3}}$	$\frac{R}{v_r}$	$\frac{L}{v_z}$	$\frac{c_{NH_3}^{inlet}}{\sum R_{NH_3}}$
Representative value	8 ms	108 ms	36 ms	9 ms	10 ms

This analysis clearly shows that radial diffusion, axial convection, and chemical reactions operate on the same timescales (order of 10 ms), while radial convection and especially axial diffusion operate on clearly longer timescales. NH_3 cracking can only be properly understood when taking all processes into account. This clearly shows the need for a 2D axisymmetric model, which includes chemical reactions, mass transport and fluid dynamics calculations, as they are all important.

The timescales in Table 2 are a useful first indication of the importance of the various processes, but to really elucidate the role of the different components, their contribution to equation (20) in section 2.4 above must be calculated. Figure 9 shows the contribution of all different processes in terms of local NH_3 production/removal, as a function of distance from the central axis and at z=1.5 cm (halfway between both electrodes).

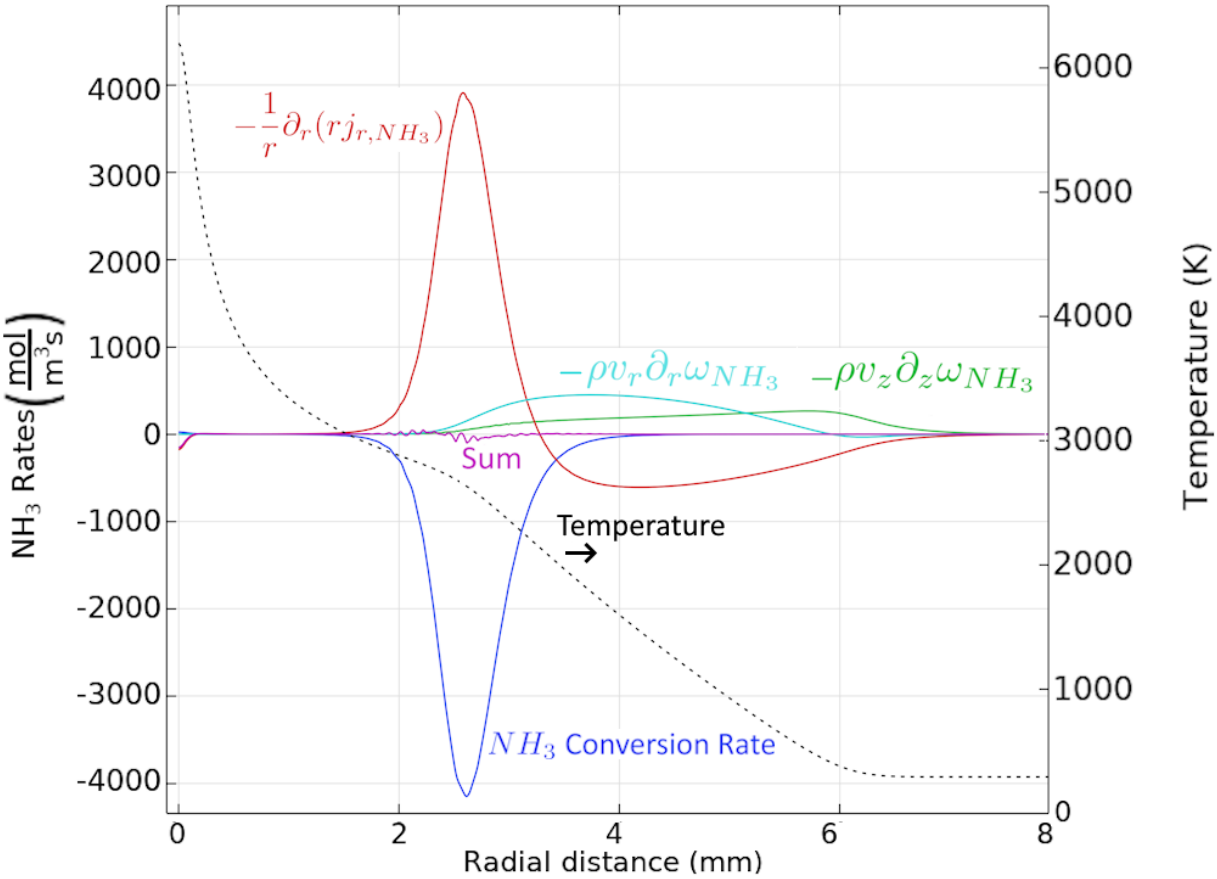

Figure 9. Calculated rates for local NH_3 production or removal (positive/negative values) as a function of radial position at z=1.5 cm, a flow rate of 15 NLM and SEI of 29 kJ/mol: the net chemical reactions (blue), r-contribution of diffusive transport (red), r-contribution of convective transport (cyan), z-contribution of convective transport (green) and the sum (purple). The z-contribution of diffusive transport does not exceed 5 $\frac{mol}{m^3 s}$ and is omitted for clarity (cf. characteristic timescale in Table 2). The temperature profile is also plotted (dashed black line, right y-axis).

Since a positive value in Figure 9 represents a local source term of NH_3 and negative represents a local sink term, we can deduce the direction of diffusion (red curve) from the figure. The diffusive term is positive in the chemically active region (r=1.7-3.2 mm) and negative further away from the plasma core (r=3.2-7 mm), hence the direction of the diffusive NH_3 flux is from the outside towards the chemically active region, where it is being converted. Below r=1.7 mm, the flux is zero, as there is no NH_3 that can reach the centre because it is all converted already. Note that the flux terms all have a minus-sign in front of their expression, as the sum of all these terms, and the NH_3 conversion rate, must add up to zero.

The chemical reactions are locally mainly balanced by diffusive transport in the radial direction, again highlighting the importance of multidimensional models, to properly calculate the transport processes. Around r = 2.6 mm convective transport starts to play an important role, by directly supplying NH_3 from the reactor edges towards the chemically active region, closer to the centre (r-transport) and by supplying 'fresh' NH_3 flowing from the inlet (z-transport). In summary, both convective and diffusive transport are essential to effectively convert the feed gas, by bringing the NH_3 towards the chemically active region.

We know from the experiments of Fedirchyk et al.[18] that the NH_3 conversion is still somewhat limited, and this is in line with our calculated results, which showed good agreement with the experimental values (see Figure 6a). Because of this good agreement, our model can identify the underlying reasons for the limited conversion. Basically speaking, to convert a higher fraction of NH_3, we need to bring more NH_3 to the chemically active region. One possible way of achieving this is by increasing the turbulent mixing, which would in turn increase the convective flux towards the hot plasma region[64]. Turbulent mixing is however not important in our setup, due to the very low turbulent kinetic energy associated with the low flow rates in this geometry (see section 2.2 above). This shows there is likely still room for improving the performance of NH_3 cracking in a reactor similar to this one, by changing the reactor design and flow profile. Our model can help to propose improvements in future work.

On the other hand, increasing the diffusion/convection towards the chemical active region will not necessarily decrease the EC of NH_3 cracking, since the latter is mainly defined by how much energy is lost to the environment, as discussed in section 3.5.3 below.

3.4 Effect of interelectrode gap

The overall conversion is defined as the relative difference of NH_3 molar flow rate through the outlet with respect to the inlet. This definition can be applied to any surface through which the total mass flux is conserved, and we apply it to cut planes parallel to the inlet. This gives rise to a spatially dependent axial conversion, given by equation (23).

$$\chi(z) = \frac{\dot{n}_{NH_3}^{in} - \int_0^R 2\pi\rho\omega_{NH_3}v_z \mathrm{r}/M_{NH_3}dr}{\dot{n}_{NH_3}^{in}} \tag{23}$$

This conversion as a function of axial position is plotted in Figure 10, for both 3 cm and 5 cm interelectrode gap. Note that the conversion at z = 13 cm and z= 15 cm, respectively, corresponds to the total reactor conversion. The current is 80 mA in both cases, which gives rise to a constant power deposition density, but the total SEI is (approximately 5/3 times) higher for 5 cm, due to the larger plasma volume. The SEI is 29 and 49 kJ/mol, for 3 and 5 cm, respectively.

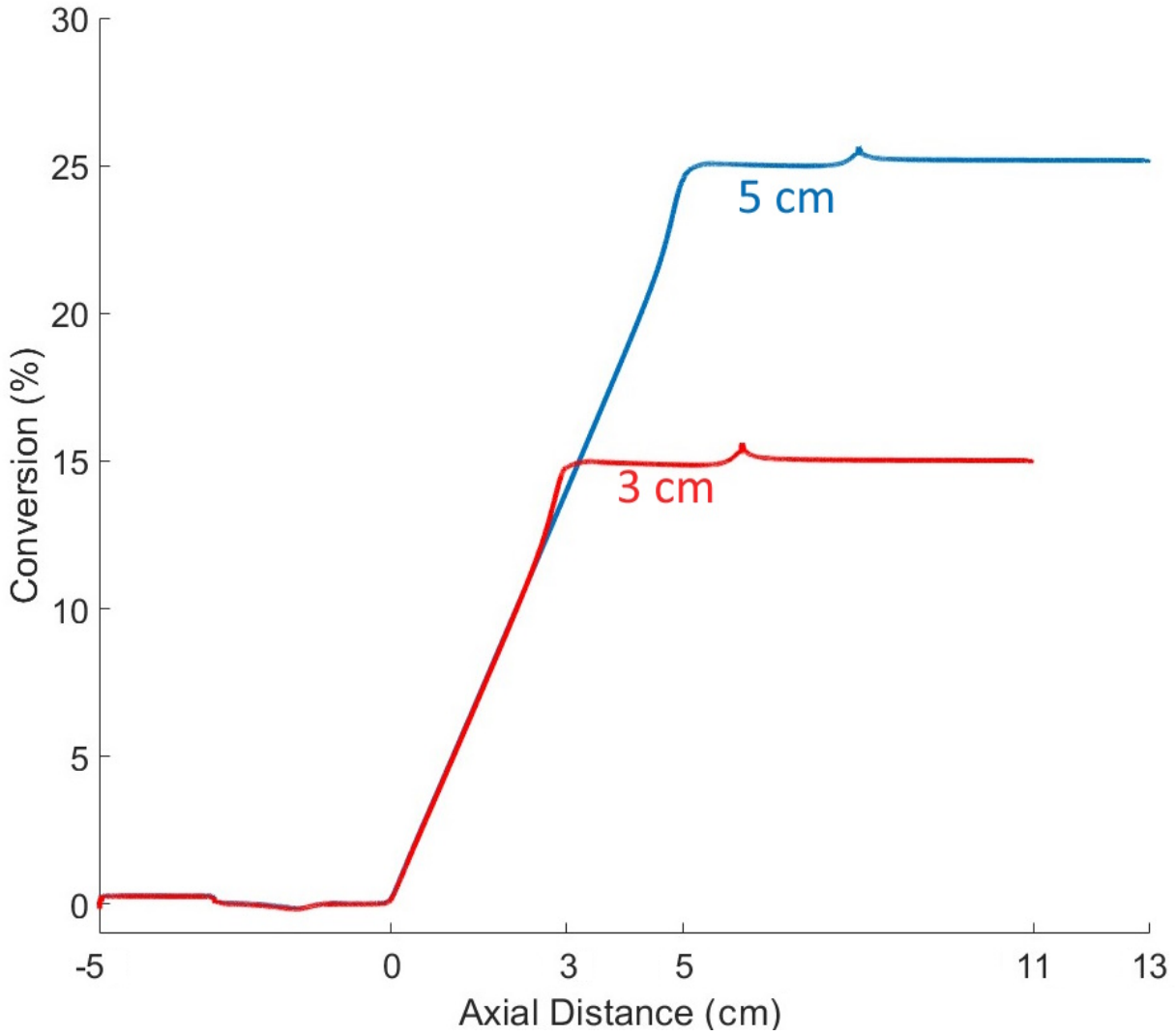

Figure 10. Conversion as a function of axial position, for 3 cm (red) and 5 cm (blue) interelectrode distance. The current is 80 mA in both cases, and the flow rate is 15 NLM, giving rise to an SEI of 29 kJ/mol and 49 kJ/mol, respectively. The axial positions indicated in the x-axis denote the inlet of the 2D model (-5 cm), the top of the powered electrode (left pin; 0) and of the ground electrode (right pin; 3 and 5 cm, respectively) and the reactor outlet (11 and 13 cm, respectively, for both interelectrode distances).

The conversion is the same for both cases until 2.4 cm, because the incoming gas sees identical flow and heat profiles up to this point. Closer to the ground electrode, the gas can no longer flow freely, and a broadening of the temperature profile occurs (see Figure 7b above). This broadening results in a higher rate of conversion (the curve inflects upward). We can see the same effect for the 5 cm gap at 4.6 cm. Our model reveals that backreactions (producing NH_3) are not important in this plasma reactor (c.f. section 3.3.1), and this is again visible in Figure 10. If backreactions were dominant, the conversion would drop once the backreaction rates become higher than the forward (NH_3 conversion) reaction rates.

The spikes visible around 6 and 8 cm are computational artifacts, due to the change in radius of the reactor (end of the ground electrode, start of the ceramic holder). The total conversion is higher

in the 5 cm case (around 25% vs 15% for the 3 cm gap), but the calculated EC is almost equal (i.e., around 197 kJ/mol), because of the different SEI. This shows that a larger interelectrode gap may improve the performance, as it leads to higher NH_3 conversion without increasing the EC. However, further experiments are needed to test this hypothesis. Moreover, the interelectrode gap cannot be increased indefinitely since this will create instabilities in the plasma. The different interelectrode distances change the relative contribution of diffusion and convection to the total amount of gas that reaches the chemically active zone. In the SI Section S.8. we show that there is more diffusion for the same SEI at larger interelectrode distances, this is compensated by a lower convective transport term.

3.5 Energy balances

To study the EC of NH_3 conversion, it is important to evaluate where the plasma energy is deposited, including the energy distribution by conduction, convection and enthalpy changes due to chemical reactions, as well as energy losses to the walls and to the electrodes.

3.5.1 Energy balance in the plasma

The energy balance equation was given in section 2.4 (equation (17)), and is repeated here for clarity:

$$-\rho C_p \vec{v} \cdot \vec{\nabla} T - \vec{\nabla} \cdot \vec{q} - \sum_{n}^{N_{react}} H_n R_n + \vec{E} \cdot \vec{J} = 0$$

The first and second term are the convective and conductive energy fluxes, the third term is the energy associated with chemical reactions, and the fourth term is the deposited energy (Joule heating). Figure 11 illustrates the relative contributions of these terms.

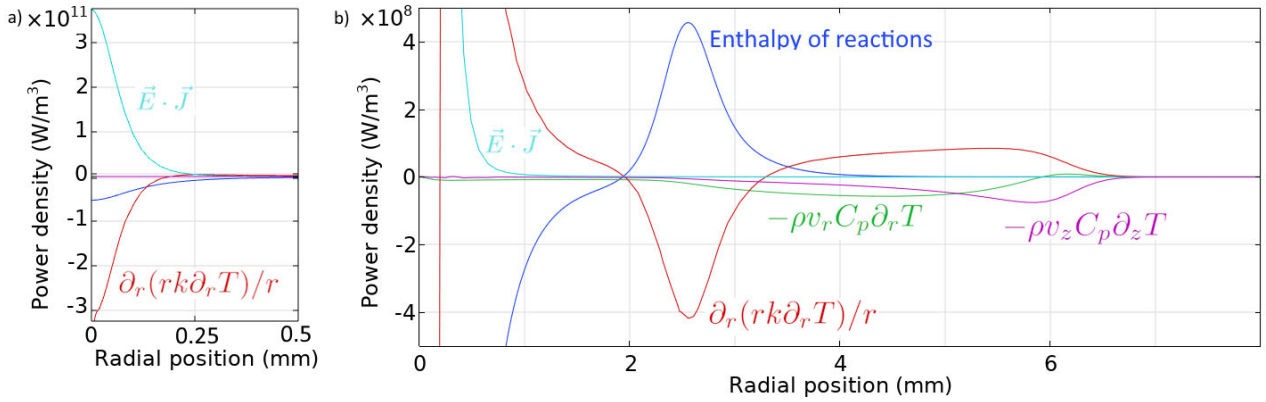

Figure 11. Local heat production or removal (positive/negative values), as a function of radial position at z=1.5 cm, a flow rate of 15 NLM, interelectrode distance of 3 cm, and SEI of 29 kJ/mol: Joule heating (cyan), radial conduction (red), enthalpy change of reactions (blue), radial convection (green), axial convection (pink). The z-contribution of conduction is omitted for clarity. Panel (a) shows the details in the centre of the plasma, while panel (b) illustrates the complete reactor. Note the different scale of the y-axis for both graphs.

More than 95% of the power is deposited very close to the centreline (cyan curve), i.e., the small current-carrying region or plasma column, within 0.3 mm of the symmetry axis. The deposited energy is partially used for the very endothermic splitting of H_2 gas into H atoms (blue curve), while the rest is radially conducted away (red curve; note that negative values indicate a local sink of energy). These three terms are the only ones visible in Figure 11a (zoomed out picture). The other contributions to the energy balance are visible in Figure 11b, where the scale of the y-axis is three orders of magnitude smaller. It must be mentioned explicitly that the 'plasma', when defined as a gas with a significant fraction of ionized molecules and free electrons, only exists in the current-carrying region very close to the centre line. However, the interesting chemistry does not depend on these electrons. As can be seen in Figure 9, all NH_3 conversion happens before the gas reaches the plasma centre. Setting the plasma centre radius (highest current-carrying region) as the half-width-half-maximum of the power deposition, as in Figure S8 in the SI, we see an inward NH_3 molar flow rate of $-5x10^{-8}$ mol/s towards the plasma centre. Therefore, no notable electron impact or thermal conversion of NH_3 will occur in the pin-to-pin plasma centre under the operating conditions investigated.

While conductive energy transport is, by definition, towards lower temperatures and thus away from the plasma column, (red curve), this term becomes positive when the influx of energy from the centre is smaller than the amount of energy transported towards the walls. In this case, the radial conduction acts as a local heat source, which occurs between r = 0.2 and 2 mm (cf. positive values). Further away from the centre, radial conductive heat transfer acts again as heat sink, because strongly exothermic reactions occur at around r = 2.5 mm. These exothermic reactions reduce the temperature gradient and redistribute heat away from the plasma centre. The sign of radial conductive heat transport changes once more and locally heats the gas from 3 mm outwards. Indeed, this is to compensate for the gas cooling in this region by convective transport (both axially and radially), which supplies fresh gas to this region. The surrounding gas acts as a thermal insulator from the cold reactor walls, and this explains why most of the energy is stored in excess heat in the gas and is not being lost at the walls (see section 3.5.3 below).

Note that in previous work[24] we used the shape of the heat source as input to the model, which can be based on measured temperature profiles or derived from light emission shapes corresponding to the plasma region. In this paper, we calculated the heat source self-consistently based on the power input and Joule heating. In the SI, section S.6, we analyse the effect of increasing the radius of the heat source, from its very contracted nature originating by Joule heating (as used in this model) to a tube-filling Gaussian profile. We found that increasing the radius from 0.07 mm (Joule heating) to 1.5 mm has almost no effect on the EC, but for larger radii the EC increases dramatically to above 400 kJ/mol. The reason of evaluating the heat source shape is because we hypothesize the important role of H atom diffusion. If the plasma core temperature drops significantly (lower than ~3200 K) the production of H atoms is severely limited. This in turn reduces the conversion and increases the EC. We will now investigate the role of these H atoms in detail.

3.5.2 Role of chemistry and H atoms in the energy balance

In Figure 11, we only considered the enthalpy changes for all reactions combined, but Figure 12 illustrates the different reactions that contribute to the overall enthalpy changes.

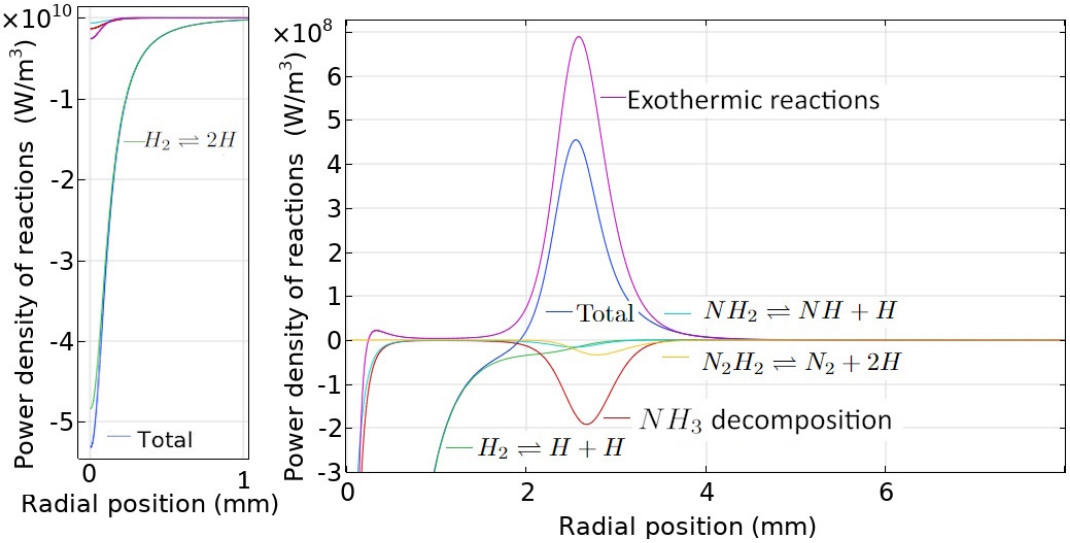

Figure 12. Local heat production or removal (positive/negative) by various chemical reactions, as a function of radial position at z=1.5 cm, a flow rate of 15 NLM, interelectrode distance of 3 cm, and SEI of 29 kJ/mol, in only the centre of the plasma (a) and the complete reactor (b); note again the different y-axis scale. Only reactions with a minimum enthalpy contribution of 10^7 W/m³ are plotted. The NH_3 decomposition reactions are R1, R2 (see Table 3 below), while the exothermic reactions are the sum of R3 to R10, also listed in Table 3.

Table 3. Reactions plotted in Figure 12. NH_3 decomposition reactions are indicated in bold. The other reactions (R3-R10) contribute to the exothermic reactions term. All reactions are equilibrium reactions, but they occur predominantly from left to right in the reactive zone.

R1	**NH_3 (+ M) ⇌ NH_2 + H (+ M)**	R6	NH_2 + NH ⇌ NH_3 + N
R2	**NH_3 + H ⇌ NH_2 + H_2**	R7	NH_2 + N ⇌ N_2 + H + H
R3	NH_2 + H ⇌ NH + H_2	R8	NH + NH ⇌ N_2 + H + H
R4	NH_2 + NH ⇌ t-N_2H_2 + H	R9	c-N_2H_2 + H ⇌ N_2 + H + H2
R5	NH_2 + NH ⇌ c-N_2H_2 + H	R10	t-N_2H_2 + H ⇌ N_2 + H + H2

At very high temperatures (close to the plasma column), a significant portion of the energy is used for splitting H_2 gas, which is a very endothermic reaction, and the H atoms diffuse away from the plasma column, as mentioned above. The H atoms then initialize several reactions. In the region

between r = 2 and 4 mm, exothermic reactions dominate. As a result, the diffusing H atoms transport heat from the plasma column outwards. It is interesting to note that even though NH_3 cracking is overall an endothermic reaction, in the region where NH_3 is destroyed, i.e., the chemically active region, the net effect of chemical reactions is exothermic. Indeed, the most important decomposition reactions are with H atoms (see Figure 10 above, as well as Table 3), which are exothermic. The NH_3 cracking in the plasma is occurring in a region with temperature between 2400 and 3000 K, as discussed in section 3.3.1, and there exists no NH_3 in the regions with temperature above 3000 K, as it is all decomposed before it arrives there via convection or diffusion. Overall, the presence of H atoms is critical for NH_3 cracking.

The flux of H atoms flowing outwards from the plasma to the chemically active region is 1.1 mmol/s. The total amount of H atoms produced by all other chemical reactions in this active region is 1.4 mmol/s. As the amount of H atoms consumed in this active region is 2.5 mmol/s, we see that there is no H atom flux to low temperature regions. The hot plasma core thus provides 44% of the total supply of H atoms to the chemically active region (the other 56% being locally produced by other chemical reactions), which significantly reduces the time needed for NH_3 conversion. Out of these 2.5 mmol/s, 64% is used for NH_3 cracking and 36% is used for NH_2 cracking. High plasma core temperatures, also beyond the threshold needed for NH_3 decomposition (for which ~3000 K is more than sufficient, see above) are therefore beneficial for the overall NH_3 cracking process, to supply H atoms (from H_2 dissociation, which needs higher temperatures) for extra NH_3 cracking.

3.5.3 Energy losses to the environment

Ideally, the deposited plasma power is exclusively used for the endothermic NH_3 cracking, but in practice, some fraction is lost. The energy loss terms are radiative losses at the quartz wall, conductive losses at the quartz wall, conductive losses at the electrodes and residual heat, which stores excess enthalpy in an elevated gas temperature. The integrals in Table 4 are calculated over the boundaries indicated in Figure 3 or (for the chemical reactions and residual heat) over the reactor volume. The residual heat is the amount of energy that a fixed chemical composition contains above 298.15 K, which can be released to the environment. This residual heat is calculated as the change in total enthalpy minus the heat of reactions. The change in total enthalpy is the total outflow of enthalpy (i.e., a weighted sum over component enthalpies integrated over the mass flow through the outlet area), minus the same quantity over the inlet (see column 1 in Table 3).

Table 4. Energy allocation in the reactor.

Residual heat	Conductive losses at electrodes	Radiative losses at quartz wall	Convective losses at quartz wall	Power to reactions ($P_{reactions}$)
$\int_{outlet} \rho v_z \sum H_i \omega_i dA$- $\int_{inlet} \rho v_z \sum H_i \omega_i dA$- $P_{reactions}$	$\int_{electrode} q_0 dA$	$\int_{wall} \epsilon \sigma_{cte} (T_{ext}^4 - T^4) dA$	$\int_{wall} h \Delta T dA$	$\int_V \sum_n^{N_{react}} \Delta H_n R_n dV$

The values in Table 4 (in W) are divided by the inlet molar flow rate (in mol/s), to obtain the energy going into each process, in kJ per mole of NH_3. The energy going to chemical reactions, residual heat and losses to the environment are presented in Figure 13, as a function of SEI.

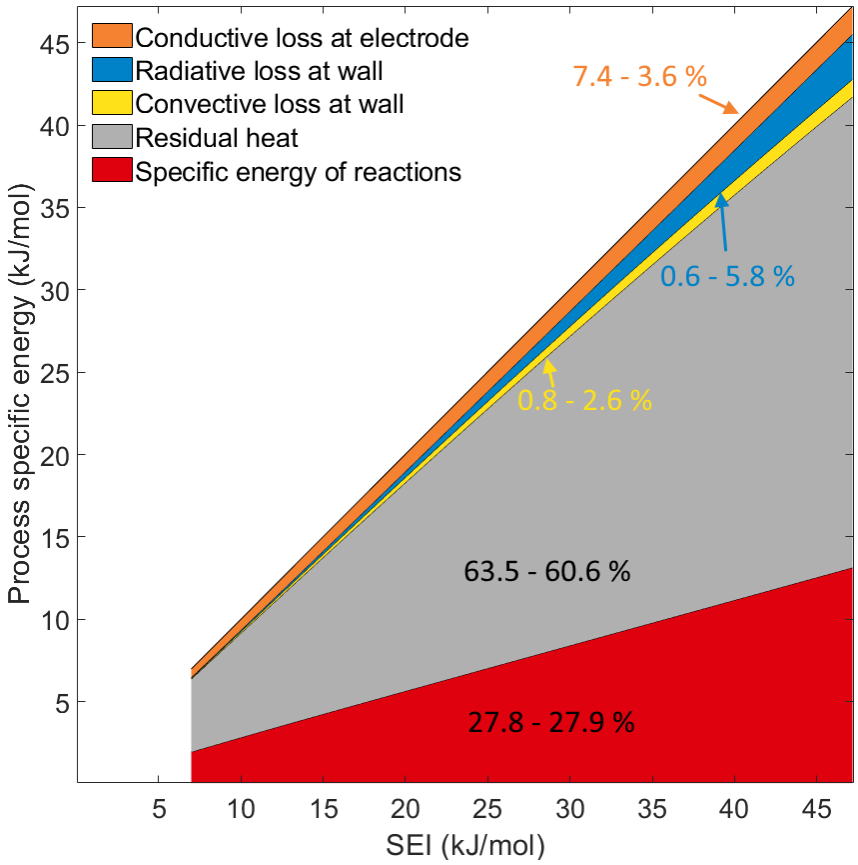

Figure 13. Fraction of the deposited specific energy used for chemical reactions (red), residual heat (grey) or losses to the environment (quartz wall or electrodes; see legend), as a function of SEI from 7.0 - 47 kJ/mol. The % contributions indicated for each process correspond to the minimal and maximal SEI value. Note that all specific energy contributions add up to the SEI. Flow rate of 20 NLM.

The most important energy term for NH_3 conversion is the energy used for chemical reactions. The larger this term, the larger the NH_3 conversion will be. All other terms are loss terms. The energy going into each separate process rises upon increasing SEI, but not at the same rate. When the SEI increases sevenfold (from 7 to 47 kJ/mol), the energy that goes to reactions increases proportionally (so the fraction is constant, around 28 %), while the residual heat increases slightly less than that (with the relative fraction decreasing from 64 to 61 %), and the losses to the electrodes also rise only to a limited extent. However, the convective and radiative losses to the quartz wall significantly increase in importance, and the radiative losses even become the second most important loss term, after the residual heat, with a relative fraction of 5.8 % at the highest SEI. This is not a surprise since the other processes scale with the linear difference between the boundary and external temperatures, while radiative losses scale with the fourth power difference, as can be seen in Table 4. The residual heat is the energy that would be most easily recovered; it is the temperature of the final mixture which is higher than room temperature but much lower than needed for any conversion to occur (400-1000 K). Hence a heat exchanger after the plasma reactor can possibly recover this excess heat. Thermally insulating the reactor walls also has the potential

to reduce the heat lost by convective and radiative transfer at this boundary. In contrast, the energy lost at the electrodes is very hard to mitigate, and only a completely different reactor design, like an electrode-free warm plasma (i.e. a microwave setup) could significantly reduce this loss term. Finally, the fact that the power to chemical reactions rises at the same rate as the SEI explains why the NH_3 conversion also rises linearly with the SEI (see Figure 6a above) and why the EC remains more or less constant over a wide range of SEI (see Figure 6b above). Both trends were also experimentally observed for the pin-to-pin reactor[18], thus validating the calculated energy balances in our model.

3.6 Possible reactor improvement

Our model identifies a couple of shortcomings in the current experimental setup. Most importantly, we did not reach full conversion of NH_3 in the investigated SEI range. For industrial applications, the NH_3 conversion should be substantially higher than the values plotted in Figure 6a above. Multiple pathways are possible to achieve this. One promising candidate is so-called reversed plasma catalysis[65], where a thermocatalyst partially converts the mixture before it comes in contact with the plasma. A second option is to increase the SEI: if the modelled trend of a nearly linear rise in conversion with increased SEI holds true, we expect full conversion at an SEI of approximately 220 kJ/mol.

In the current set-up, however, the predicted wall temperature at very high SEI would lead to annealing or melting of the quartz wall. To prevent this, one could either increase the radius of the quartz tube or add cooling to this wall. If the cooling would be combined with heat integration, this might decrease the EC by recycling energy. One could also change the quartz wall material by a metal. This would improve the thermal stability of the reactor wall at high operating powers and might introduce catalytic effects on the reactor wall.

Two effects explain the increased conversion for the 5 cm inter-electrode case. While it does not have a significantly larger proportion of convective gas flow into the plasma region compared to a 3 cm inter-electrode distance at similar current (see SI, section S.8), there is a significantly higher power deposition due to the larger volume over which we deposit power. Secondly, because the region is bigger, there is more time for diffusive effects to carry untreated gas into a region where conversion occurs. To be specific, the amount of unconverted NH_3 that flows into the chemically reactive zone via diffusion with a 3 or 5 cm inter-electrode distance is 1.4 mmol/s and 2.4 mmol/s, respectively, for a current of 80 mA. Hence, increasing diffusion via a highly turbulent flow may also be a possibility for a future reactor improvement.

Finally, one could put multiple plasma reactors in parallel. While this will not change the conversion or EC of a single reactor, it does increase the H_2 production rate, as recently demonstrated for CO_2 conversion by placing several warm plasma reactors in parallel[66].

4 Conclusion

We developed a novel, fully self-consistent 2D axisymmetric model for a pin-to-pin low-current plasma arc reactor used for NH_3 cracking, for green H_2 production. For the first time, the power deposition profile in a multidimensional NH_3 plasma model is calculated self-consistently by

properly taking Joule heating into account. The model only needs a few external parameters as input, namely the reactor geometry, gas flow rate and composition at the inlet, the applied current and rate coefficients of the chemical reactions, while all other quantities are calculated self-consistently. The fact that we use no fitting parameters significantly increases the applicability of this model for reactor design improvements in future work.

Our model predicts full NH_3 conversion in the temperature region between 2400 and 3000 K, i.e., the so-called chemically active region. The overall degree of conversion is determined by three main factors, (i) how wide the chemically active region is, (ii) how much NH_3 is transported towards this chemically active region, and (iii) how many H atoms diffuse from the central plasma column to this chemically active zone. To adequately capture all these determining factors, a 2D model with sufficiently advanced flow characteristics, as developed in this work, is necessary. Our model also predicts that there are no significant backreactions, thus eliminating the need for fast quenching in an NH_3 plasma cracking reactor, unlike for CO_2 conversion or NO_x formation[61,62]

Our model shows good agreement with experimental results for the NH_3 conversion and corresponding EC as a function of SEI, without any fitting during any point of development. Therefore, it can be used to reveal the underlying mechanisms in this pin-to-pin reactor and suggest possible improvements in future work. It provides useful information on the gas flow profile, which first follows a vortex flow around the electrode pin near the inlet and then becomes nearly laminar in the region between both pin electrodes. Furthermore, the calculated temperature profile exhibits a maximum of about 6000 K at the symmetry axis, and the chemically active region is located around 2.5 mm from the symmetry axis.

We also discuss in detail the chemical pathways, and the transport processes, both of species and energy. The transport of species can explain the limited conversion (found experimentally and confirmed by our model) in this pin-to-pin reactor. Our model reveals that this might be improved by more turbulence, so that more NH_3 and H would be transported to the chemically active region. However, turbulence is limited in this reactor. Hence, future reactor design could focus on increasing the turbulence, for better mixing of NH_3 and H into the chemically active region. Furthermore, the insights obtained by our model on the transport of energy allow us to better understand how the deposited power is distributed over several processes, like chemical reactions, but also residual gas heat and losses to the environment. Likewise, we discuss possible adaptations to reduce these loss terms, which can also guide future reactor development. Most compelling is to include heat recovery, to reduce the loss of residual gas heat. This will be investigated in our future work.

Acknowledgements

This work was supported by the HyPACT project, funded by the Belgian Energy Transition Fund, as well as by the Excellence of Science FWO-FNRS project (FWO grant ID G0I1822N; EOS ID 40007511) and the European Research Council (ERC) under the European Union's Horizon 2020 research and innovation programme (grant agreement No. 810182–SCOPE ERC Synergy project).

CRediT authorship contribution statement

Rubén Quiroz Marnef: Conceptualization, Formal analysis, Investigation, Methodology, Validation, Visualization, Writing - original draft, Writing – review and editing

Stein Maerivoet: Conceptualization, Formal analysis, Investigation, Methodology, Validation, Visualization, Writing - original draft, Writing – review and editing

Ivan Tsonev: Conceptualization, Formal analysis, Investigation, Methodology, Validation, Supervision, Writing - review and editing

François Reniers: Funding acquisition, Supervision, Project administration, Writing – review and editing

Annemie Bogaerts: Conceptualization, Funding acquisition, Methodology, Resources, Supervision, Project administration, Writing – review and editing

References

1. Commission, E. & Action, D.-G. for C. Going Climate-Neutral by 2050 – A Strategic Long-Term Vision for a Prosperous, Modern, Competitive and Climate-Neutral EU Economy. (Publications Office, 2019).

2. Falcone, P. M., Hiete, M. & Sapio, A. Hydrogen economy and sustainable development goals: Review and policy insights. Curr. Opin. Green Sustain. Chem. **31**, 100506 (2021).

3. Hren, R. et al. Hydrogen production, storage and transport for renewable energy and chemicals: An environmental footprint assessment. Renew. Sustain. Energy Rev. **173**, 113113 (2023).

4. Aziz, M., Wijayanta, A. T. & Nandiyanto, A. B. D. Ammonia as Effective Hydrogen Storage: A Review on Production, Storage and Utilization. Energies **13**, 3062 (2020).

5. IRENA and AEA. Innovation Outlook: Renewable Ammonia. Ammon. Energy Assoc. (2022).

6. Trangwachirachai, K., Rouwenhorst, K., Lefferts, L. & Faria Albanese, J. A. Recent progress on ammonia cracking technologies for scalable hydrogen production. Curr. Opin. Green Sustain. Chem. **49**, 100945 (2024).

7. Zecher-Freeman, N., Zong, H., Xie, P. & Wang, C. Catalytic cracking of ammonia toward carbon-neutral liquid fuel. Curr. Opin. Green Sustain. Chem. **44**, 100860 (2023).

8. Asif, M. et al. Recent advances in green hydrogen production, storage and commercial-scale use via catalytic ammonia cracking. Chem. Eng. J. **473**, 145381 (2023).

9. Gorbanev, Y., Fedirchyk, I. & Bogaerts, A. Plasma catalysis in ammonia production and decomposition: Use it, or lose it? Curr. Opin. Green Sustain. Chem. **47**, 100916 (2024).

10. Hayakawa, Y., Kambara, S. & Miura, T. Hydrogen production from ammonia by the plasma membrane reactor. Int. J. Hydrog. Energy **45**, 32082–32088 (2020).

11. Andersen, J. A., Christensen, J. M., Østberg, M., Bogaerts, A. & Jensen, A. D. Plasma-catalytic ammonia decomposition using a packed-bed dielectric barrier discharge reactor. Int. J. Hydrog. Energy **47**, 32081–32091 (2022).

12. Wang, L. et al. Highly Dispersed Co Nanoparticles Prepared by an Improved Method for Plasma-Driven NH3 Decomposition to Produce H2. Catalysts **9**, (2019).

13. Młotek, M., Perron, M. & Krawczyk, K. Ammonia Decomposition in a Gliding Discharge Plasma. Energy Technol. **9**, 2100677 (2021).

14. Zhao, Y., Wang, L., Zhang, J., Gong, W. & Guo, H. Decomposition of ammonia by atmospheric pressure AC discharge: Catalytic effect of the electrodes. Catal. Today **211**, 72–77 (2013).

15. Lin, Q. F. et al. Instantaneous hydrogen production from ammonia by non-thermal arc plasma combining with catalyst. Energy Rep. **7**, 4064–4070 (2021).

16. Ronduda, H. et al. Cobalt catalysts for COx-free hydrogen production: Effect of catalyst type on ammonia decomposition in gliding discharge plasma reactor. J. CO2 Util. **82**, 102755 (2024).

17. Zhang, X. & Cha, M. S. Ammonia cracking for hydrogen production using a microwave argon plasma jet. J. Phys. Appl. Phys. **57**, 065203 (2023).

18. Fedirchyk, I., Tsonev, I., Quiroz Marnef, R. & Bogaerts, A. Plasma-assisted NH3 cracking in warm plasma reactors for green H2 production. Chem. Eng. J. **499**, 155946 (2024).

19. Bang, S., Snoeckx, R. & Cha, M. S. Kinetic Study for Plasma Assisted Cracking of NH3: Approaches and Challenges. J. Phys. Chem. A **127**, 1271–1282 (2023).

20. Andersen, J. A. et al. Ammonia decomposition in a dielectric barrier discharge plasma: Insights from experiments and kinetic modeling. Chem. Eng. Sci. **271**, 118550 (2023).

21. Arakoni, R. A., Bhoj, A. N. & Kushner, M. J. H2 generation in Ar/NH3 microdischarges. J. Phys. Appl. Phys. **40**, 2476 (2007).

22. Bayer, B. N., Bhan, A. & Bruggeman, P. J. Reaction Pathways and Energy Consumption in NH3 Decomposition for H2 Production by Low Temperature, Atmospheric Pressure Plasma. Plasma Chem. Plasma Process. (2024) doi:10.1007/s11090-024-10501-8.

23. NIST (2010) Standard Reference Database 69: NIST Chemistry WebBook; National Institute of Standards and Technology, (n.d.).

24. Maerivoet, S., Tsonev, I., Slaets, J., Reniers, F. & Bogaerts, A. Coupled multi-dimensional modelling of warm plasmas: Application and validation for an atmospheric pressure glow discharge in CO2/CH4/O2. Chem. Eng. J. **492**, 152006 (2024).

25. Cruccolini, V. et al. Multidimensional modeling of non-equilibrium plasma generated by a radio-frequency corona discharge. Plasma Sources Sci. Technol. **29**, 115013 (2020).

26. Bukowski, J. D., Graves, D. B. & Vitello, P. Two-dimensional fluid model of an inductively coupled plasma with comparison to experimental spatial profiles. J. Appl. Phys. **80**, 2614–2623 (1996).

27. Bogaerts, A. et al. CO2 conversion by plasma technology: insights from modeling the plasma chemistry and plasma reactor design. Plasma Sources Sci. Technol. **26**, 063001 (2017).

28. Chein, R.-Y., Chen, Y.-C., Chang, C.-S. & Chung, J. N. Numerical modeling of hydrogen production from ammonia decomposition for fuel cell applications. Int. J. Hydrog. Energy **35**, 589–597 (2010).

29. Chiuta, S., Everson, R. C., Neomagus, H. W. J. P. & Bessarabov, D. G. Hydrogen production from ammonia decomposition over a commercial Ru/Al2O3 catalyst in a microchannel reactor: Experimental validation and CFD simulation. Int. J. Hydrog. Energy **41**, 3774–3785 (2016).

30. Liebermann, M. & Lichtenberg, A. Plasma Dynamics. in Principles of Plasma Discharges and Materials Processing 87–132 (John Wiley & Sons, Ltd, 2005).

31. Tatar, M. et al. Analysis of a plasma reactor performance for direct nitrogen fixation by use of three-dimensional simulations and experiments. Chem. Eng. J. **497**, 154756 (2024).

32. Wanten, B., Vertongen, R., De Meyer, R. & Bogaerts, A. Plasma-based CO2 conversion: How to correctly analyze the performance? J. Energy Chem. **86**, 180–196 (2023).

33. COMSOL Multiphysics®. CFDModuleUsersGuide.pdf. (2023).

34. Panton, R. L. Incompressible Flow. in Incompressible Flow 851–868 (John Wiley & Sons, Ltd, 2013).

35. Menter, F., Kuntz, M. & Langtry, R. Ten years of industrial experience with the SST turbulence model turbulence heat and mass transfer. in Proceedings of the 4th International

Symposium on Turbulence, Heat and Mass Transfer, edited by: Hanjalic, K., Nagano, Y., and Tummers, MJ 625–632.

36. Taylor, J. R. Classical Mechanics. (University Science Books, 2005).

37. Tsonev, I., Boothroyd, J., Kolev, S. & Bogaerts, A. Simulation of glow and arc discharges in nitrogen: effects of the cathode emission mechanisms. Plasma Sources Sci. Technol. **32**, 054002 (2023).

38. COMSOL Multiphysics®. AC/DC Module User's Guide. (2023).

39. Petrov, V. & Reznik, V. Measurement of the emissivity of quartz glass. High Temp.-High Press. **v. 4**, 687–693 (1972).

40. Bang, S., Maerivoet, S., Reniers, F. & Bogaerts, A. Plasma-based NH3 cracking: A better insight in the performance by chemical kinetics modelling. Submitted to Green Chem.

41. Itikawa, Y. Cross Sections for Electron Collisions with Nitrogen Molecules. J. Phys. Chem. Ref. Data **35**, 31–53 (2005).

42. Itikawa. Itikawa database, www.lxcat.net, retrieved on March 20, 2024. (2024).

43. L.L. Alves, '"The IST-Lisbon database on LXCat"' J. Phys. Conf. Series 2014, 565, 1.

44. A. Schmalzried, A. Luque and N. Lehtinen, IAA Database on lxcat, www.lxcat.net/IAA, August 2023,I nstituto de Astrofísica de Andalucía.

45. Morgan database, www.lxcat.net, retrieved on March 20, 2024.

46. Hayashi database, www.lxcat.net, retrieved on March 20, 2024.

47. McBride, B., Zehe, M. & Gordon, S. NASA Glenn coefficients for calculating thermodynamic properties of individual species. (2002).

48. Goodwin, D. G., Moffat, H. K., Schoegl, I., Speth, R. L. & Weber, B. W. Cantera: An Object-oriented Software Toolkit for Chemical Kinetics, Thermodynamics, and Transport Processes. (2023).

49. Benilov, M. S. & Naidis, G. V. Modelling of low-current discharges in atmospheric-pressure air taking account of non-equilibrium effects. J. Phys. Appl. Phys. **36**, 1834 (2003).

50. COMSOL Multiphysics®. Chemical Reaction Engineering Module User's Guide. (2023).

51. Kee, R. J., Coltrin, M. E., Glarborg, P. & Coltrin, M. E. Chemically Reacting Flow: Theory and Practice. (Wiley Interscience, Hoboken, NJ, 2003).

52. COMSOL Multiphysics®. Heat Transfer Module User's guide. (2023).

53. Wilke, C. R. A Viscosity Equation for Gas Mixtures. J. Chem. Phys. **18**, 517–519 (1950).

54. Naidis, G. V. Simulation of convection-stabilized low-current glow and arc discharges in atmospheric-pressure air. Plasma Sources Sci. Technol. **16**, 297 (2007).

55. Akishev, Y., Grushin, M., Karalnik, V., Petryakov, A. & Trushkin, N. On basic processes sustaining constricted glow discharge in longitudinal N_2 flow at atmospheric pressure. J. Phys. Appl. Phys. **43**, 215202 (2010).

56. COMSOL Multiphysics®. COMSOL Reference Manual. (2023).

57. Tsonev, I., Eshtehardi, H. A., Delplancke, M.-P. & Bogaerts, A. Importance of geometric effects in scaling up energy-efficient plasma-based nitrogen fixation. Sustain. Energy Fuels **8**, 2191–2209 (2024).

58. Alturaifi, S. A., Mathieu, O. & Petersen, E. L. An experimental and modeling study of ammonia pyrolysis. Combust. Flame **235**, 111694 (2022).

59. Glarborg, P., Hashemi, H. & Marshall, P. Challenges in Kinetic modeling of ammonia pyrolysis. Fuel Commun. **10**, 100049 (2022).

60. Siddiqui, M. S., Rasheed, A., Kvamsdal, T. & Tabib, M. Effect of Turbulence Intensity on the Performance of an Offshore Vertical Axis Wind Turbine. Energy Procedia **80**, 312–320 (2015).

61. da Silva, C. L. et al. The Plasma Nature of Lightning Channels and the Resulting Nonlinear Resistance. J. Geophys. Res. Atmospheres **124**, 9442–9463 (2019).

62. MATLAB Version 23.2.0.2459199 (R2023b) Update 5. (The Mathworks, Inc., Natick, Massachusetts, 2023).

63. Weiland, C. Mechanics of Flow Similarities. (Springer Cham, 2020).

64. Sreenivasan, K. R. Turbulent mixing: A perspective. Proc. Natl. Acad. Sci. **116**, 18175–18183 (2019).

65. Van Steenweghen, F. et al. Reversed Plasma Catalysis Process Design for Efficient Ammonia Decomposition. ACS Sustain. Chem. Eng. (2025)

66. O'Modhrain, C., Trenchev, G., Gorbanev, Y. & Bogaerts, A. Upscaling Plasma-Based CO2 Conversion: Case Study of a Multi-Reactor Gliding Arc Plasmatron. ACS Eng. Au **4**, 333–344 (2024).

Supporting Information: Spatially resolved modelling of NH_3 cracking in warm plasma

Rubén Quiroz Marnef*[1], Stein Maerivoet*[1,2], Ivan Tsonev[1], Francois Reniers[2] and Annemie Bogaerts[1]

[1] Research group PLASMANT, Department of Chemistry, University of Antwerp, Universiteitsplein 1, BE-2610 Wilrijk-Antwerp, Belgium
[2] Chemistry of Surfaces, Interfaces and Nanomaterials, Faculty of Sciences, Université Libre de Bruxelles, CP255, Avenue F.D. Roosevelt 50, B-1050 Brussels, Belgium

* These authors contributed equally to the work

E-mail: ruben.quirozmarnef@uantwerpen.be; stein.maerivoet@uantwerpen.be; annemie.bogaerts@uantwerpen.be

S.1. All boundary conditions of the 2D model

Figure S1 presents the entire geometry of the pin-to-pin reactor, like Figure 3 of the main paper, but with the numbers of the boundaries indicated, to help the reader understand Table S1.

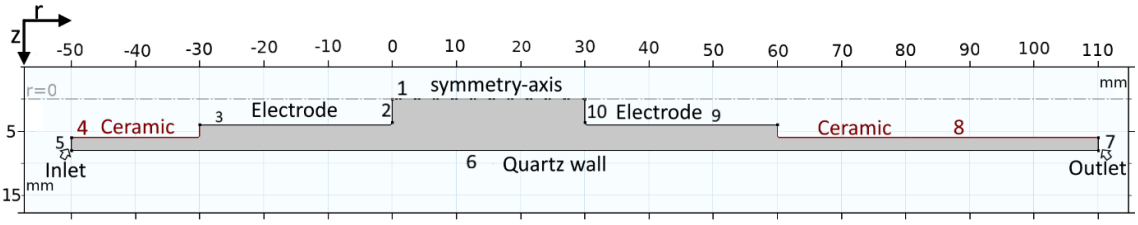

Figure S1 Geometry with boundaries numbered.

Table S1 Overview of all boundary conditions in the 2D model (see numbers of the boundaries in Figure S1). ΔH is the sensible enthalpy (kJ/mol), σ_{SB} is the Stefan-Boltzmann constant (W/(m^2 K^4)), T_{ext} is the external temperature (293.15 K), ϵ is the emissivity of quartz (dimensionless).

Boundary	Heat transfer	Electrical Currents	Gas flow	Chemistry
1	Axial symmetry	Axial symmetry	$v_r = 0$ $v_\phi = 0$	Axial symmetry
2	Thermal insulation $\vec{n} \cdot \vec{q} = 0$	Terminal $\int_{\partial\Omega} \vec{J} \cdot \vec{n}\, dS = I_0$ The integral runs over boundary 2 and 3	No slip wall $\vec{v} = 0$	No flux $-\vec{n} \cdot \vec{J_i} = 0$

3	Heat flux $-\vec{n} \cdot \vec{q} = q_0$ $q_0 = h\Delta T$ $h = 20\frac{W}{Km^2}$	Terminal $\int_{\partial\Omega} \vec{J} \cdot \vec{n}\, dS = I_0$ The integral runs over boundary 2 and 3	No slip wall $\vec{v} = 0$	No flux $-\vec{n} \cdot \vec{J_i} = 0$
4,8	Thermal insulation $\vec{n} \cdot \vec{q} = 0$	Electrical Insulation $\vec{n} \cdot \vec{J} = 0$	No slip wall $\vec{v} = 0$	No flux $-\vec{n} \cdot \vec{J_i} = 0$
5	Inflow $-\vec{n} \cdot \vec{q} = \rho\Delta H\, \vec{v} \cdot \vec{n}$ $\Delta H = \int_{T_{ext}}^{T} C_p dT$	Electrical Insulation $\vec{n} \cdot \vec{J} = 0$	Inlet $v_r = v_{r_0}$ $v_\phi = v_{\phi_0}$ $v_z = v_{z_0}$	Inflow $\omega_i = \omega_{i_0}$
6	Heat flux $-\vec{n} \cdot \vec{q} = q_0$ $q_0 = h\Delta T + \epsilon\sigma_{SB}(T_{ext}^4 - T^4)$ h for external natural convection[1,2] $\epsilon = 0.75$[3]	Electrical Insulation $\vec{n} \cdot \vec{J} = 0$	No slip wall $\vec{v} = 0$	No flux $-\vec{n} \cdot \vec{J_i} = 0$
7	Thermal insulation $\vec{n} \cdot \vec{q} = 0$	Electrical Insulation $\vec{n} \cdot \vec{J} = 0$	Outlet $[-p\boldsymbol{I} + \boldsymbol{K}]\, \vec{n} = 0$	No diffusion-flux $-\vec{n} \cdot \rho D_i^m \vec{\nabla}\omega_i = 0$
9	Heat flux $-\vec{n} \cdot \vec{q} = q_0$ $q_0 = h\Delta T$ $h = 20\frac{W}{Km^2}$	Ground $V = 0$	No slip wall $\vec{v} = 0$	No flux $-\vec{n} \cdot \vec{J_i} = 0$
10	Thermal insulation $\vec{n} \cdot \vec{q} = 0$	Ground $V = 0$	No slip wall $\vec{v} = 0$	No flux $-\vec{n} \cdot \vec{J_i} = 0$

S.2. Thermodynamic equilibrium data

The thermodynamic equilibrium of a thermal system, which is just dependent on T_g, will at high enough gas temperatures, yield electrons from associative ionization. This is complemented with an electron density, which is used to calculate the electrical conductivity of an equilibrated system. While the real conductivity in the plasma system, which is subject to an external electric field, will be different, we use the equilibrium electrical conductivity in the 2D axisymmetric model, as we do not have the computational power to solve the electron energy balance combined with all other physics included in the model. Naidis et al[4] reported that the differences between non-LTE-calculated and LTE-calculated conductivities were small at high currents (>50 mA). As expected, the Joule heating heat source shape will differ depending on the electrical conductivity of the system. However, section S.7. in this SI presents an analysis of the effect of the heat source shape on the main plasma metrics, from which we see that some deviation of the heat source shape, and thus of the electrical conductivity, will not influence the plasma metrics, as long as the total deposited energy is equal.

Figure S2 shows the temperature-dependent electrical conductivity used to calculate the electrical current and heat deposited (see section 2.4 in the main paper). The electrical current is extremely low for temperatures below 1500 K as there are almost no electrons below this temperature. The conductivity increases exponentially with temperature, as expected.

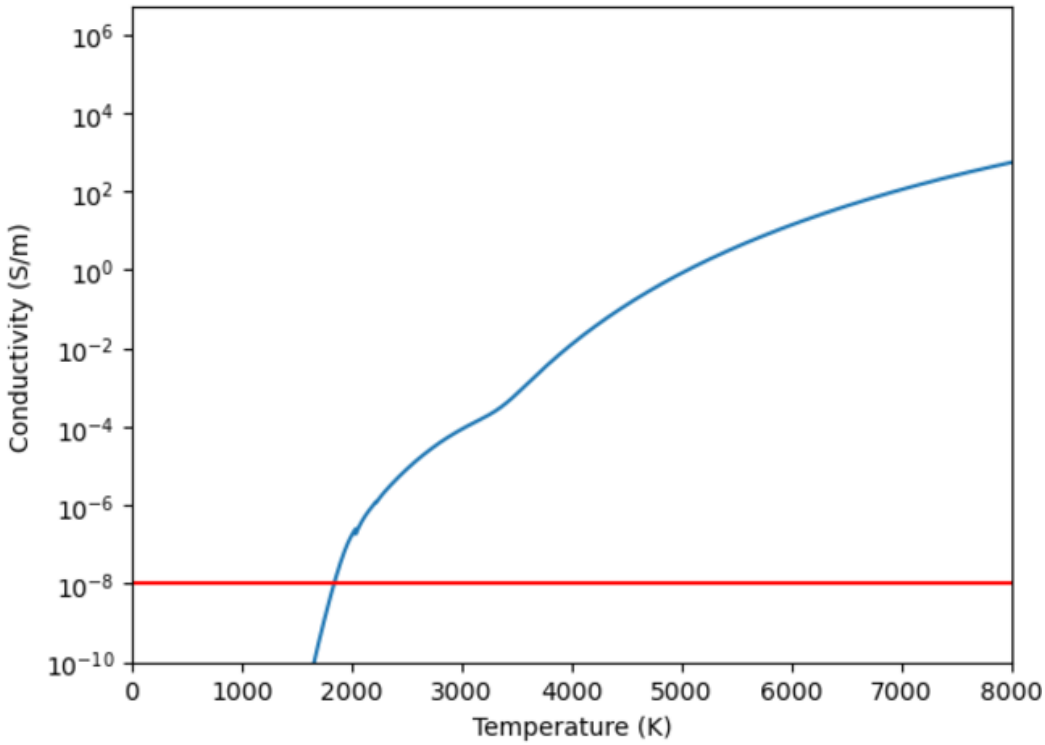

Figure S2. Electrical conductivity for NH_3 at thermal equilibrium, as a function of temperature. The red line is the lower bound used for numerical stability.

Figure S3 presents the molar fractions at thermodynamics equilibrium, as a function of temperature, both on a linear scale (a) and on a logarithmic scale (b). We can see that NH_3 is unstable at elevated temperatures, while the ionization degree is quite low over the full

temperature range (maximum 2.2x10^{-3} at 8000 K). This information is used to calculate the conductivity, as mentioned in section 2.4 of the main paper.

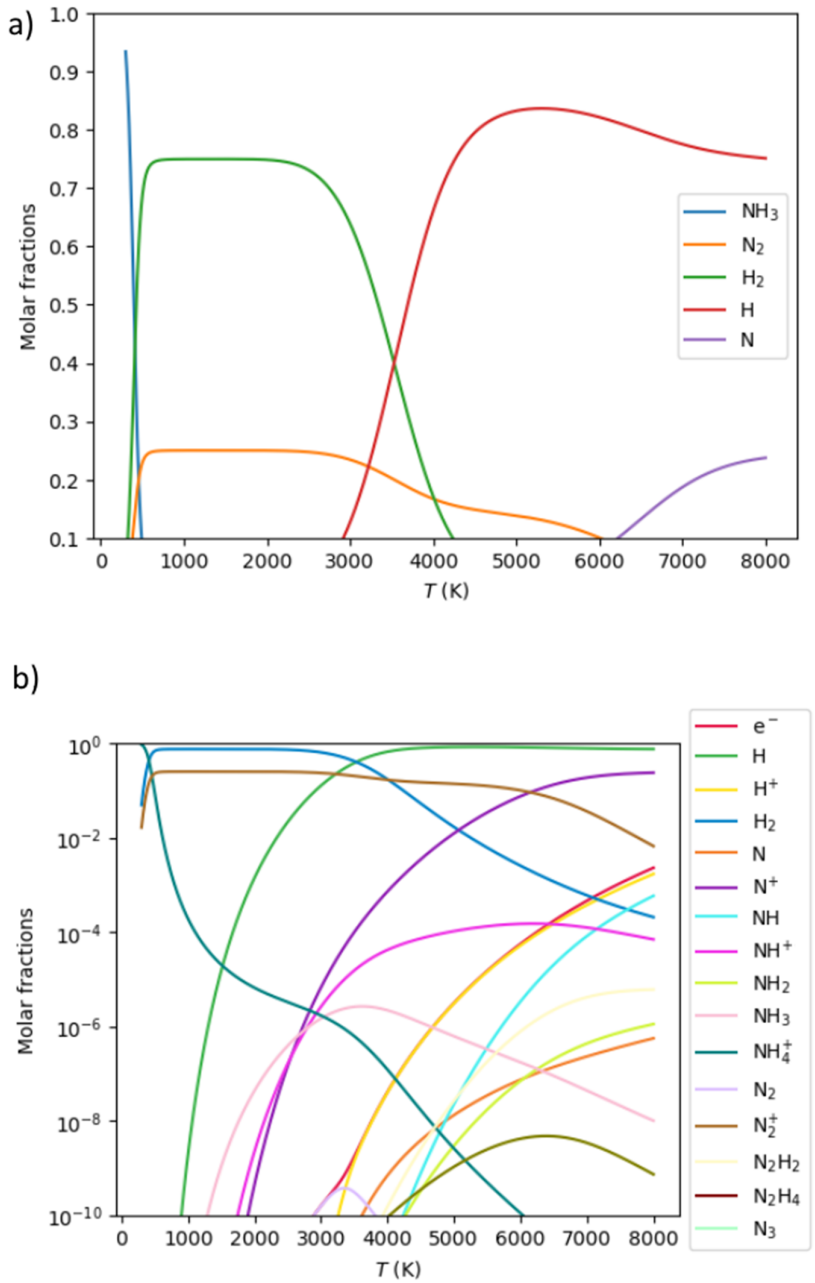

Figure S3. Thermodynamic equilibrium molar fractions as a function of temperature, on a linear scale (a, showing only the dominant species) and a logarithmic scale (b, presenting also the minor species).

S.3. Viscosity comparison

The viscosity used in our work is shown together with the calculations by Colombo et al. for pure Nitrogen plasma.

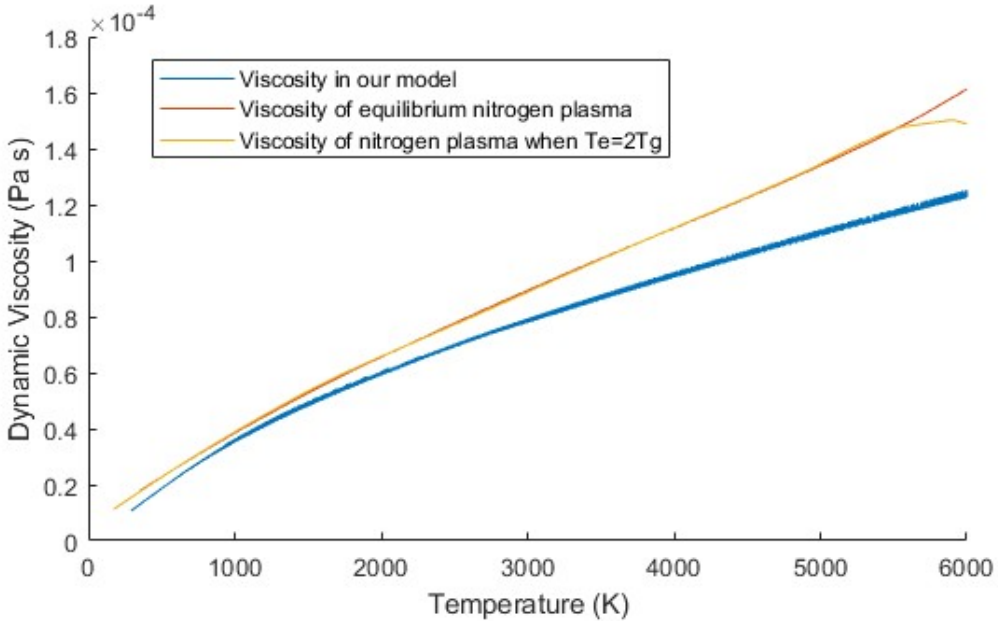

Figure S4. Viscosity used in our work (blue) compared to the values of a pure nitrogen plasma as calculated by Colombo et al.[5]

As one can see, the viscosity we used closely aligns with the more involved plasma viscosities calculated by Colombo et al. The small deviation is caused by the contribution of the hydrogen fraction in the plasma mixture.

S.4. Full and reduced chemistry set

Table S2 lists all chemical reactions, and their rate coefficients, as well as the corresponding references, for the complete thermal NH_3 set, which is used to obtain the reduced chemistry set, and the latter is summarized in Table S3, for the operating conditions of the warm plasma pin-to-pin reactor. For both sets all reactions are detailed balanced, see Maerivoet et al. for further information[6] For other plasma types, it is important to start again from the full set, as the chemistry reduction depends on certain parameters specific for each plasma reactor (such as maximum temperature, quenching rate, residence time…). The reduction method is similar to the one in Maerivoet et al.[6] and is described in section S.5. The reactions that are part of the reduced chemistry set, are also indicated in Table S2 in bold and with asterisk (*).

Table S2 Full set of chemical reactions, their rate coefficients and corresponding references. The reactions present in the reduced chemistry set are indicated in bold and with asterisk. The units of the rate coefficients are also denoted. NNH is included as a species, but it is removed in the reduced set and replaced by N_2 + H.

Reaction	Rate coefficient	Ref.
1*) $NH_2 + H (+ M) \rightleftharpoons NH_3 (+ M)$	See rate equation in footnote [a], with: $k_0 = 3.0 \times 10^{10} \cdot \left(\frac{T_g}{1K}\right)^{-1.9} \frac{m^6}{mol^2 s}$ $k_\infty = 1.5 \times 10^8 \cdot \left(\frac{T_g}{1K}\right)^{0.167} \frac{m^3}{mol\ s}$ $F_c = 0.5$ $N_{2\ eff} = 2.5$	7
2*) $NH_3 + H \rightleftharpoons NH_2 + H_2$	$5.4 \times 10^{-1} \cdot \left(\frac{T_g}{1K}\right)^{2.4} \cdot exp\left(\frac{-4.149 \times 10^4\ \mathrm{J/mol}}{R_{const} \cdot T_g}\right) \frac{m^3}{mol\ s}$	8
3*) $NH + H + M \rightleftharpoons NH_2 + M$	$1.2 \times 10^{13} \cdot \left(\frac{T_g}{1K}\right)^{-2.71} \frac{m^6}{mol^2\ s}$	9
4*) $NH_2 + H \rightleftharpoons NH + H_2$	$5.1 \times 10^2 \cdot \left(\frac{T_g}{1K}\right)^{1.5} \cdot exp\left(\frac{-1.548 \times 10^4\ \mathrm{J/mol}}{R_{const} \cdot T_g}\right) \frac{m^3}{mol\ s}$	7
5*) $NH_2 + NH_2 \rightleftharpoons NH_3 + NH$	$5.6 \times 10^{-6} \cdot \left(\frac{T_g}{1K}\right)^{3.53} \cdot exp\left(\frac{-2.310\ \times 10^3\ \mathrm{J/mol}}{R_{const} \cdot T_g}\right) \frac{m^3}{mol\ s}$	10
6) $NH_2 + NH_2 \rightleftharpoons t\text{-}N_2H_2 + H_2$	$1.7 \times 10^2 \cdot \left(\frac{T_g}{1K}\right)^{1.02} \cdot exp\left(\frac{-49.3\ \times 10^3\ \mathrm{J/mol}}{R_{const} \cdot T_g}\right) \frac{m^3}{mol\ s}$	10
7) $NH_2 + NH_2 \rightleftharpoons H_2NN + H_2$	$7.2 \times 10^{-2} \cdot \left(\frac{T_g}{1K}\right)^{1.88} \cdot exp\left(\frac{-36.83\ \times 10^3\ \mathrm{J/mol}}{R_{const} \cdot T_g}\right) \frac{m^3}{mol\ s}$	10
8) $NH_2 + NH_2 (+ M) \rightleftharpoons N_2H_4 (+ M)$	See rate equation in footnote [a], with: $k_0 = 1.6 \times 10^{22} \cdot \left(\frac{T_g}{1K}\right)^{-5.49} \cdot exp\left(\frac{-8.31\ \times 10^3\ \mathrm{J/mol}}{R_{const} \cdot T_g}\right) \frac{m^6}{mol^2 s}$ $k_\infty = 5.6 \times 10^8 \cdot \left(\frac{T_g}{1K}\right)^{-0.414} \cdot exp\left(\frac{-276\ \mathrm{J/mol}}{R_{const} \cdot T_g}\right) \frac{m^3}{mol\ s}$ $F_c = 0.31$	10
9*) $NH_2 + NH \rightleftharpoons t\text{-}N_2H_2 + H$	$1.2 \times 10^9 \cdot \left(\frac{T_g}{1K}\right)^{-0.5} \frac{m^3}{mol\ s}$	11
10*) $NH_2 + NH \rightleftharpoons c\text{-}N_2H_2 + H$	$3.0 \times 10^8 \cdot \left(\frac{T_g}{1K}\right)^{-0.5} \frac{m^3}{mol\ s}$	11
11*) $NH_2 + NH \rightleftharpoons NH_3 + N$	$9.6 \times 10^{-3} \cdot \left(\frac{T_g}{1K}\right)^{2.46} \cdot exp\left(\frac{-4.477 \times 10^2\ J/mol}{R_{const} \cdot T_g}\right) \frac{m^3}{mol\ s}$	10
12*) $NH_2 + N \rightleftharpoons N_2 + H + H$	$7 \times 10^7 \frac{m^3}{mol\ s}$	12
13) $NH + M \rightleftharpoons N + H + M$	$1.8 \times 10^8 \cdot exp\left(\frac{-313 \times 10^3\ J/mol}{R_{const} \cdot T_g}\right) \frac{m^3}{mol\ s}$	9
14) $NH + H \rightleftharpoons N + H_2$	$3.49 \times 10^7 \cdot \left(\frac{T_g}{1K}\right)^{-0.52} \cdot exp\left(\frac{-144 \times 10^3\ J/mol}{R_{const} \cdot T_g}\right) \frac{m^3}{mol\ s}$	13
15*) $NH + NH \rightleftharpoons NNH + H$	$6.2 \times 10^7 \cdot \left(\frac{T_g}{1K}\right)^{-0.036} \cdot exp\left(\frac{6.736 \times 10^2\ J/mol}{R_{const} \cdot T_g}\right) \frac{m^3}{mol\ s}$	10
16) $NH + NH \rightleftharpoons NH_2 + N$	$5.7 \times 10^{-7} \cdot \left(\frac{T_g}{1K}\right)^{3.88} \cdot exp\left(\frac{-1.430 \times 10^3\ J/mol}{R_{const} \cdot T_g}\right) \frac{m^3}{mol\ s}$	10
17*) $NH + N \rightleftharpoons N_2 + H$	$1.17 \times 10^7 \cdot \left(\frac{T_g}{1K}\right)^{0.51} \cdot exp\left(\frac{-80\ \mathrm{J/mol}}{R_{const} \cdot T_g}\right) \frac{m^3}{mol\ s}$	14

18*) $H_2 + M \rightleftharpoons H + H + M$	$4.6 \times 10^{13} \cdot \left(\frac{T_g}{1K}\right)^{-1.4} \cdot exp\left(\frac{-4.367 \times 10^5\ J/mol}{R_{const} \cdot T_g}\right) \frac{m^3}{mol\ s}$ $H_{2\ eff} = 2.5$	15
19) $N_2H_3 + H (+ M) \rightleftharpoons N_2H_4 (+ M)$	See rate equation in footnote [a], with: $k_0 = 3.6 \times 10^{10} \cdot \left(\frac{T_g}{1K}\right)^{-1.76} \frac{m^6}{mol^2 s}$ $k_\infty = 1.6 \times 10^8 \frac{m^3}{mol\ s}$ $F_c = 0.5$	7
20) $N_2H_4 + H \rightleftharpoons N_2H_3 + H_2$	$2.7 \times 10^{13} \cdot \left(\frac{T_g}{1K}\right)^{2.56} \cdot exp\left(\frac{-5.1 \times 10^3\ J/mol}{R_{const} \cdot T_g}\right) \frac{m^3}{mol\ s}$	16
21) $N_2H_4 + NH_2 \rightleftharpoons N_2H_3 + NH_3$	$2 \times 10^{-5} \cdot \left(\frac{T_g}{1K}\right)^{3.62} \cdot exp\left(\frac{1.66 \times 10^3\ J/mol}{R_{const} \cdot T_g}\right) \frac{m^3}{mol\ s}$	17
22*) $N_2H_3 (+ M) \rightleftharpoons t\text{-}N_2H_2 + H (+ M)$	See rate equation in footnote [b], with: $k_0 = 3.8 \times 10^{34} \cdot \left(\frac{T_g}{1K}\right)^{-6.88} \cdot exp\left(\frac{-2.279 \times 10^5 J/mol}{R_{const} \cdot T_g}\right) \frac{m^3}{mol\ s}$ $k_\infty = 1.3 \times 10^{11} \cdot \left(\frac{T_g}{1K}\right)^{0.819} \cdot exp\left(\frac{-2.011 \times 10^5\ J/mol}{R_{const} \cdot T_g}\right) \frac{1}{s}$ $F_c = (1 - 0.168) \cdot exp\left(\frac{-T_g}{80000\ \mathrm{K}}\right)$ $+ 0.168 \cdot exp\left(\frac{-T_g}{28\ \mathrm{K}}\right) + exp\left(\frac{-7298\ \mathrm{K}}{T_g}\right)$ $N_{2\ eff} = 2$	18
23) $N_2H_3 + H \rightleftharpoons t\text{-}N_2H_2 + H_2$	$4.6 \times 10^{-5} \cdot \left(\frac{T_g}{1K}\right)^{3.53} \cdot exp\left(\frac{-15.69 \times 10^3\ J/mol}{R_{const} \cdot T_g}\right) \frac{m^3}{mol\ s}$	19
24) $N_2H_3 + H \rightleftharpoons c\text{-}N_2H_2 + H_2$	$2.7 \times 10^{-4} \cdot \left(\frac{T_g}{1K}\right)^{3.18} \cdot exp\left(\frac{-27.7 \times 10^3\ J/mol}{R_{const} \cdot T_g}\right) \frac{m^3}{mol\ s}$	19
25) $N_2H_3 + H \rightleftharpoons H_2NN + H_2$	$3.1 \times 10^{0} \cdot \left(\frac{T_g}{1K}\right)^{2.11} \cdot exp\left(\frac{-9.54 \times 10^2\ J/mol}{R_{const} \cdot T_g}\right) \frac{m^3}{mol\ s}$	19
26*) $N_2H_3 + H \rightleftharpoons NH_2 + NH_2$	$1.0 \times 10^8 \frac{m^3}{mol\ s}$	19
27) $N_2H_3 + NH_2 \rightleftharpoons t\text{-}N_2H_2 + NH_3$	$6.1 \times 10^{-7} \cdot \left(\frac{T_g}{1K}\right)^{3.574} \cdot exp\left(\frac{-5 \times 10^3\ J/mol}{R_{const} \cdot T_g}\right) \frac{m^3}{mol\ s}$	18
28) $N_2H_3 + NH_2 \rightleftharpoons H_2NN + NH_3$	$1.1 \times 10^{-5} \cdot \left(\frac{T_g}{1K}\right)^{3.080} \cdot exp\left(\frac{-8.83 \times 10^2\ J/mol}{R_{const} \cdot T_g}\right) \frac{m^3}{mol\ s}$	18
29) $N_2H_3 + NH \rightleftharpoons t\text{-}N_2H_2 + NH_2$	$2 \times 10^7 \frac{m^3}{mol\ s}$	7
30*) $t\text{-}N_2H_2 \rightleftharpoons c\text{-}N_2H_2$ £ (twisting)	See rate equation in footnote [b], with: $k_0 = 2.3 \times 10^{23} \cdot \left(\frac{T_g}{1K}\right)^{-4} \cdot exp\left(\frac{-2.515 \times 10^5\ J/mol}{R_{const} \cdot T_g}\right) \frac{m^3}{mol\ s}$ $k_\infty = 1.5 \times 10^8 \cdot exp\left(\frac{-2.30 \times 10^5 J/mol}{R_{const} \cdot T_g}\right) \frac{1}{s}$ $F_c = (1 - 0.35) \cdot exp\left(\frac{-T_g}{650\ \mathrm{K}}\right) + 0.35 \cdot exp\left(\frac{-T_g}{10600\ \mathrm{K}}\right)$	19
31*) $t\text{-}N_2H_2 (+ M) \rightleftharpoons c\text{-}N_2H_2 (+ M)$ (bending)	See rate equation in footnote [b], with: $k_0 = 3.0 \times 10^{22} \cdot \left(\frac{T_g}{1K}\right)^{-3.56} \cdot exp\left(\frac{-2.347 \times 10^5\ J/mol}{R_{const} \cdot T_g}\right) \frac{m^3}{mol\ s}$	19

	$k_\infty = 4.9 \times 10^9 \cdot \left(\frac{T_g}{1K}\right)^{1.18} \cdot exp\left(\frac{-1.996 \times 10^5 J/mol}{R_{const} \cdot T_g}\right)\frac{1}{s}$ $F_c = (1 - 0.35) \cdot exp\left(\frac{-T_g}{650\ \mathrm{K}}\right) + 0.35 \cdot exp\left(\frac{-T_g}{10600\ \mathrm{K}}\right)$	
32*) t-N_2H_2 + H ⇌ NNH + H_2	$9.6 \times 10^1 \cdot \left(\frac{T_g}{1K}\right)^{1.8} \cdot exp\left(\frac{-3.766 \times 10^3 J/mol}{R_{const} \cdot T_g}\right)\frac{m^3}{mol\ s}$	19
33*) t-N_2H_2 + NH_2 ⇌ NNH + NH_3	$2.7 \times 10^{-1} \cdot \left(\frac{T_g}{1K}\right)^{2.226} \cdot exp\left(\frac{4.326 \times 10^3 J/mol}{R_{const} \cdot T_g}\right)\frac{m^3}{mol\ s}$	18
34*) t-N_2H_2 + NH ⇌ NNH + NH_2	$2.4 \times 10^0 \cdot \left(\frac{T_g}{1K}\right)^{2.0} \cdot exp\left(\frac{5 \times 10^3 J/mol}{R_{const} \cdot T_g}\right)\frac{m^3}{mol\ s}$	20
35*) c-N_2H_2 (+ M) ⇌ NNH + H (+ M)	See rate equation in footnote [b], with: $k_0 = 9.6 \times 10^{29} \cdot \left(\frac{T_g}{1K}\right)^{-5.44} \cdot exp\left(\frac{-2.674 \times 10^5 J/mol}{R_{const} \cdot T_g}\right)\frac{m^3}{mol\ s}$ $k_\infty = 5.7 \times 10^{16} \cdot exp\left(\frac{-2.456 \times 10^5\ J/mol}{R_{const} \cdot T_g}\right)\frac{1}{s}$ $F_c = (1 - 0.44) \cdot exp\left(\frac{-T_g}{520\ \mathrm{K}}\right) + 0.44 \cdot exp\left(\frac{-T_g}{6150\ \mathrm{K}}\right)$	19
36*) c-N_2H_2 + H ⇌ NNH + H_2	$2.8 \times 10^2 \cdot \left(\frac{T_g}{1K}\right)^{1.720} \cdot exp\left(\frac{-1.966 \times 10^3 J/mol}{R_{const} \cdot T_g}\right)\frac{m^3}{mol\ s}$	19
37) c-N_2H_2 + H ⇌ t-N_2H_2 + H	$7.8 \times 10^2 \cdot \left(\frac{T_g}{1K}\right)^{1.58} \cdot exp\left(\frac{-9.12 \times 10^3 J/mol}{R_{const} \cdot T_g}\right)\frac{m^3}{mol\ s}$	19
38) H_2NN ⇌ NNH + H	$3.4 \times 10^{18} \cdot \left(\frac{T_g}{1K}\right)^{-4.83} \cdot exp\left(\frac{-1.93 \times 10^5 J/mol}{R_{const} \cdot T_g}\right)\frac{m^3}{mol\ s}$	20
39*) H_2NN ⇌ N_2 + H_2	$2.5 \times 10^{14} \cdot exp\left(\frac{-2.209 \times 10^5}{R_{const} \cdot T_g}\right)\frac{1}{s}$	21
40) H_2NN + H ⇌ NNH + H_2	$4.8 \times 10^2 \cdot \left(\frac{T_g}{1K}\right)^{1.5} \cdot exp\left(\frac{3.74 \times 10^3 J/mol}{R_{const} \cdot T_g}\right)\frac{m^3}{mol\ s}$	20
41) H_2NN + H ⇌ t-N_2H_2 + H	$7.0 \times 10^7 \frac{m^3}{mol\ s}$	20
42) H_2NN + NH_2 ⇌ NNH + NH_3	$1.8 \times 10^0 \cdot \left(\frac{T_g}{1K}\right)^{1.94} \cdot exp\left(\frac{4.82 \times 10^3 J/mol}{R_{const} \cdot T_g}\right)\frac{m^3}{mol\ s}$	20
43) NNH ⇌ N_2 + H	$6.35 \times 10^7 \cdot \left(\frac{T_g}{298K}\right)^{-0.53} \cdot exp\left(\frac{1.18 \times 10^5 J/mol}{R_{const} \cdot T_g}\right)\frac{m^3}{mol\ s}$	14
44) NNH + H ⇌ N_2 + H_2	$3.99 \times 10^7 \cdot \left(\frac{T_g}{298K}\right)^{0.17} \frac{m^3}{mol\ s}$	22
45) NNH + NH ⇌ N_2 + NH_2	$5 \times 10^7 \frac{m^3}{mol\ s}$	7
46) NNH + NH_2 ⇌ N_2 + NH_3	$5 \times 10^7 \frac{m^3}{mol\ s}$	7
47*) t-N_2H_2 (+ M) ⇌ NNH + H (+ M)	See rate equation in footnote [b], with: $k_0 = 8.7 \times 10^{33} \cdot \left(\frac{T_g}{1K}\right)^{-6.91} \cdot exp\left(\frac{-2.946 \times 10^5 J/mol}{R_{const} \cdot T_g}\right)\frac{m^3}{mol\ s}$ $k_\infty = 6.3 \times 10^{16} \cdot exp\left(\frac{-2.678 \times 10^5}{R_{const} \cdot T_g}\right)\frac{1}{s}$ $F_c = (1 - 0.44) \cdot exp\left(\frac{-T_g}{520\ \mathrm{K}}\right) + 0.44 \cdot exp\left(\frac{-T_g}{6150\ \mathrm{K}}\right)$	19

48) $N_2H_4 + M \rightleftharpoons H_2NN + H_2 + M$	PLOG rate (see [20]): $k_{0.1\text{bar}} = 4 \times 10^{38} \cdot \left(\frac{T_g}{1K}\right)^{-9.85} \cdot exp\left(\frac{-3 \times 10^5 J/mol}{R_{const} \cdot T_g}\right)\frac{m^3}{mol\ s}$ $k_{1\text{bar}} = 5.3 \times 10^{33} \cdot \left(\frac{T_g}{1K}\right)^{-8.35} \cdot exp\left(\frac{-2.9 \times 10^5 J/mol}{R_{const} \cdot T_g}\right)\frac{m^3}{mol\ s}$ $k_{10\text{bar}} = 2.5 \times 10^{33} \cdot \left(\frac{T_g}{1K}\right)^{-8.2} \cdot exp\left(\frac{-2.9 \times 10^5 J/mol}{R_{const} \cdot T_g}\right)\frac{m^3}{mol\ s}$	20
49*) $N_2H_4 + H \rightleftharpoons NH_3 + NH_2$	$3.0 \times 10^0 \cdot \left(\frac{T_g}{1K}\right)^{2.070} \cdot exp\left(\frac{-3.352 \times 10^4}{R_{const} \cdot T_g}\right)\frac{m^3}{mol\ s}$	17
50*) $N_2 + M \rightleftharpoons N + N + M$	$3.0 \times 10^{10} \cdot exp\left(\frac{-9.412 \times 10^5\ J/mol}{R_{const} \cdot T_g}\right) \cdot \left(1 - exp\left(\frac{-2.789 \times 10^4\ J/mol}{R_{const} \cdot T_g}\right)\right)\frac{m^3}{mol\ s}$ $N_{2\,eff} = 2.2$	23

[a] NNH in these reactions was substituted for N_2 and H, as discussed in the main paper

[b] Notes: a falloff expression, Lindemann-Hinshelwood expression with broadening factor:

$$k = \frac{k_0[M]k_\infty}{k_0[M] + k_\infty}F; \log F = \frac{\log F_c}{1 + \left[\frac{\log(k_0[M]/k_\infty)}{N}\right]^2}; N = 0.75 - 1.27 \log F_c$$

Table S3 Reduced set of chemical reactions, their rate coefficients and corresponding references. The units of the rate coefficients are also denoted. NNH is replaced by N_2 + H as a species.

Reaction	Rate coefficient	Ref.
1) $NH_2 + H (+ M) \rightleftharpoons NH_3 (+ M)$	See rate equation in footnote [a], with: $k_0 = 3.0 \times 10^{10} \cdot \left(\frac{T_g}{1K}\right)^{-1.9} \frac{m^6}{mol^2 s}$ $k_\infty = 1.5 \times 10^{8} \cdot \left(\frac{T_g}{1K}\right)^{0.167} \frac{m^3}{mol\ s}$ $F_c = 0.5$ $N_{2\,eff} = 2.5$	7
2) $NH_3 + H \rightleftharpoons NH_2 + H_2$	$5.4 \times 10^{-1} \cdot \left(\frac{T_g}{1K}\right)^{2.4} \cdot exp\left(\frac{-4.149 \times 10^4\ \mathrm{J/mol}}{R_{const} \cdot T_g}\right) \frac{m^3}{mol\ s}$	8
3) $NH + H + M \rightleftharpoons NH_2 + M$	$1.2 \times 10^{13} \cdot \left(\frac{T_g}{1K}\right)^{-2.71} \frac{m^6}{mol^2\ s}$	9
4) $NH_2 + H \rightleftharpoons NH + H_2$	$5.1 \times 10^{2} \cdot \left(\frac{T_g}{1K}\right)^{1.5} \cdot exp\left(\frac{-1.548 \times 10^4\ \mathrm{J/mol}}{R_{const} \cdot T_g}\right) \frac{m^3}{mol\ s}$	7
5) $NH_2 + NH_2 \rightleftharpoons NH_3 + NH$	$5.6 \times 10^{-6} \cdot \left(\frac{T_g}{1K}\right)^{3.53} \cdot exp\left(\frac{-2.310\ \times 10^3\ \mathrm{J/mol}}{R_{const} \cdot T_g}\right) \frac{m^3}{mol\ s}$	10
6) $NH_2 + NH \rightleftharpoons t\text{-}N_2H_2 + H$	$1.2 \times 10^{9} \cdot \left(\frac{T_g}{1K}\right)^{-0.5} \frac{m^3}{mol\ s}$	11
7) $NH_2 + NH \rightleftharpoons c\text{-}N_2H_2 + H$	$3.0 \times 10^{8} \cdot \left(\frac{T_g}{1K}\right)^{-0.5} \frac{m^3}{mol\ s}$	11
8) $NH_2 + NH \rightleftharpoons NH_3 + N$	$9.6 \times 10^{-3} \cdot \left(\frac{T_g}{1K}\right)^{2.46} \cdot exp\left(\frac{-4.477 \times 10^2\ J/mol}{R_{const} \cdot T_g}\right) \frac{m^3}{mol\ s}$	10
9) $NH_2 + N \rightleftharpoons N_2 + H + H$	$7 \times 10^{7} \frac{m^3}{mol\ s}$	12
10) $NH + NH \rightleftharpoons N_2 + H + H$ [a]	$6.2 \times 10^{7} \cdot \left(\frac{T_g}{1K}\right)^{-0.036} \cdot exp\left(\frac{6.736 \times 10^2\ J/mol}{R_{const} \cdot T_g}\right) \frac{m^3}{mol\ s}$	10
11) $NH + N \rightleftharpoons N_2 + H$	$6.402 \times 10^{5} \cdot \left(\frac{T_g}{1K}\right)^{0.51} \cdot exp\left(\frac{-80\ \mathrm{J/mol}}{R_{const} \cdot T_g}\right) \frac{m^3}{mol\ s}$	14
12) $H_2 + M \rightleftharpoons H + H + M$	$4.6 \times 10^{13} \cdot \left(\frac{T_g}{1K}\right)^{-1.4} \cdot exp\left(\frac{-4.367 \times 10^5\ J/mol}{R_{const} \cdot T_g}\right) \frac{m^3}{mol\ s}$ $H_{2\,eff} = 2.5$	15
13) $N_2H_3 (+ M) \rightleftharpoons t\text{-}N_2H_2 + H (+ M)$	See rate equation in footnote [b], with: $k_0 = 3.8 \times 10^{34} \cdot \left(\frac{T_g}{1K}\right)^{-6.88} \cdot exp\left(\frac{-2.279 \times 10^5 J/mol}{R_{const} \cdot T_g}\right) \frac{m^3}{mol\ s}$ $k_\infty = 1.3 \times 10^{11} \cdot \left(\frac{T_g}{1K}\right)^{0.819} \cdot exp\left(\frac{-2.011 \times 10^5\ J/mol}{R_{const} \cdot T_g}\right) \frac{1}{s}$ $F_c = (1 - 0.168) \cdot exp\left(\frac{-T_g}{80000\ \mathrm{K}}\right) + 0.168 \cdot exp\left(\frac{-T_g}{28\ \mathrm{K}}\right) + exp\left(\frac{-7298\ \mathrm{K}}{T_g}\right)$ $N_{2\,eff} = 2$	18
14) $N_2H_3 + H \rightleftharpoons NH_2 + NH_2$	$1.0 \times 10^{8} \frac{m^3}{mol\ s}$	19

15) t-N_2H_2 (+ M) ⇌ c-N_2H_2 (+ M)	See rate equation in footnote [b], with: $k_0 = 3.0 \times 10^{22} \cdot \left(\frac{T_g}{1K}\right)^{-3.56} \cdot exp\left(\frac{-2.347 \times 10^5\ J/mol}{R_{const} \cdot T_g}\right)\frac{m^3}{mol\ s}$ $k_\infty = 4.9 \times 10^9 \cdot \left(\frac{T_g}{1K}\right)^{1.18} \cdot exp\left(\frac{-1.996 \times 10^5 J/mol}{R_{const} \cdot T_g}\right)\frac{1}{s}$ $F_c = (1 - 0.35) \cdot exp\left(\frac{-T_g}{650\ \mathrm{K}}\right) + 0.35 \cdot exp\left(\frac{-T_g}{10600\ \mathrm{K}}\right)$	19
16) t-N_2H_2 + H ⇌ N_2 + H + H_2 [a]	$9.6 \times 10^1 \cdot \left(\frac{T_g}{1K}\right)^{1.8} \cdot exp\left(\frac{-3.766 \times 10^3 J/mol}{R_{const} \cdot T_g}\right)\frac{m^3}{mol\ s}$	19
17) t-N_2H_2 + NH_2 ⇌ N_2 + H + NH_3 [a]	$2.7 \times 10^{-1} \cdot \left(\frac{T_g}{1K}\right)^{2.226} \cdot exp\left(\frac{4.326 \times 10^3 J/mol}{R_{const} \cdot T_g}\right)\frac{m^3}{mol\ s}$	18
18) c-N_2H_2 (+ M) ⇌ N_2 + H + H [a] (+ M)	See rate equation in footnote [b], with: $k_0 = 9.6 \times 10^{29} \cdot \left(\frac{T_g}{1K}\right)^{-5.44} \cdot exp\left(\frac{-2.674 \times 10^5 J/mol}{R_{const} \cdot T_g}\right)\frac{m^3}{mol\ s}$ $k_\infty = 5.7 \times 10^{16} \cdot exp\left(\frac{-2.456 \times 10^5\ J/mol}{R_{const} \cdot T_g}\right)\frac{1}{s}$ $F_c = (1 - 0.44) \cdot exp\left(\frac{-T_g}{520\ \mathrm{K}}\right) + 0.44 \cdot exp\left(\frac{-T_g}{6150\ \mathrm{K}}\right)$	19
19) c-N_2H_2 + H ⇌ N_2 + H + H_2 [a]	$2.8 \times 10^2 \cdot \left(\frac{T_g}{1K}\right)^{1.720} \cdot exp\left(\frac{-1.966 \times 10^3 J/mol}{R_{const} \cdot T_g}\right)\frac{m^3}{mol\ s}$	19
20) H_2NN ⇌ N_2 + H_2	$2.5 \times 10^{14} \cdot exp\left(\frac{-2.209 \times 10^5}{R_{const} \cdot T_g}\right)\frac{1}{s}$	20
21) t-N_2H_2 (+ M) ⇌ N_2 + H + H (+ M) [a]	See rate equation in footnote [b], with: $k_0 = 8.7 \times 10^{33} \cdot \left(\frac{T_g}{1K}\right)^{-6.91} \cdot exp\left(\frac{-2.946 \times 10^5 J/mol}{R_{const} \cdot T_g}\right)\frac{m^3}{mol\ s}$ $k_\infty = 6.3 \times 10^{16} \cdot exp\left(\frac{-2.678 \times 10^5}{R_{const} \cdot T_g}\right)\frac{1}{s}$ $F_c = (1 - 0.44) \cdot exp\left(\frac{-T_g}{520\ \mathrm{K}}\right) + 0.44 \cdot exp\left(\frac{-T_g}{6150\ \mathrm{K}}\right)$	19
22) N_2H_4 + H ⇌ NH_3 + NH_2	$3.0 \times 10^0 \cdot \left(\frac{T_g}{1K}\right)^{2.070} \cdot exp\left(\frac{-3.352 \times 10^4}{R_{const} \cdot T_g}\right)\frac{m^3}{mol\ s}$	17
23) N_2 + M ⇌ N + N + M	$3.0 \times 10^{10} \cdot exp\left(\frac{-9.412 \times 10^5\ J/mol}{R_{const} \cdot T_g}\right) \cdot \left(1 - exp\left(\frac{-2.789 \times 10^4\ J/mol}{R_{const} \cdot T_g}\right)\right)\frac{m^3}{mol\ s}$ $N_{2\,eff} = 2.2$	23

[a] NNH in these reactions was substituted for N_2 and H, as discussed in the text.

[b] Notes: a falloff expression, Lindemann-Hinshelwood expression with broadening factor:

$$k = \frac{k_0[M]k_\infty}{k_0[M] + k_\infty}F; \log F = \frac{\log F_c}{1 + \left[\frac{\log(k_0[M]/k_\infty)}{N}\right]^2}; N = 0.75 - 1.27 \log F_c$$

S.5. Chemistry reduction

S.5.1. Methodology

The full workflow is shown in figure S5. We ran multiple simulations with a 0D model for an extensive gas temperature range (1200 K to 6000 K) and an extensive range of starting conditions (ranging from pure NH_3 to diluted NH_3, i.e., 10 % NH_3 in 90 % N_2 or 10 % NH_3 in 90 % H_2), see top of the figure. We incorporate temperatures up to 6000 K in our initial reduction of the NH_3 chemistry, so that our chemical kinetics scheme is valid in the entire range. As can be seen in the main manuscript, in Figure 7, almost all NH_3 conversion will occur between a temperature range of 2400 to 3000 K, and thus, any decomposition of 100 % NH_3 with a starting temperature of 3200 K or higher does not reflect a real location in the pin-to-pin reactor under these conditions. Instead, we do this to allow the reduced model to be applicable for other reactors, which might heat NH_3 faster, so that the NH_3 gas could reach higher temperatures.

In each iteration, we omitted a single reaction from the reaction kinetics set and we calculated the deviation on the output, as the effect of omitting this one single reaction on the full unmodified set. The deviation is the maximum difference between the original set and the single reaction reduced set at any point in time for each species. For instance, reactions Q, R, S and T could have deviations y, x, z and w, respectively. After each reaction receives a deviation score, they are sorted from least important (lowest score) to most important (highest score). So, if $w < x < y < z$, then we sort their impact as $T < R < Q < S$. Finally, we run additional simulations, removing multiple reactions based on the previous sorted deviation scores, from low impact to high. Four groups might then be identified, i.e., 1. “only T removed as least impactful”, 2. “R and T removed as the two least impactful”, etc. This leaves 50 sets of simulations for various conditions, each with one more reaction omitted than the previous one. The final reduced set is chosen based on the maximum allowed deviation at any point in the simulation compared to the full, unmodified set, which was set in this case to have an absolute deviation of 0.1 %. In the example case, if the simulation ran without T and R would yield a deviation score of 0.08 % and the simulation without Q, T and R would yield 0.12 %, the resulting set would omit species R and T but not Q. Our final reduced set consists of 13 species and 23 reactions.

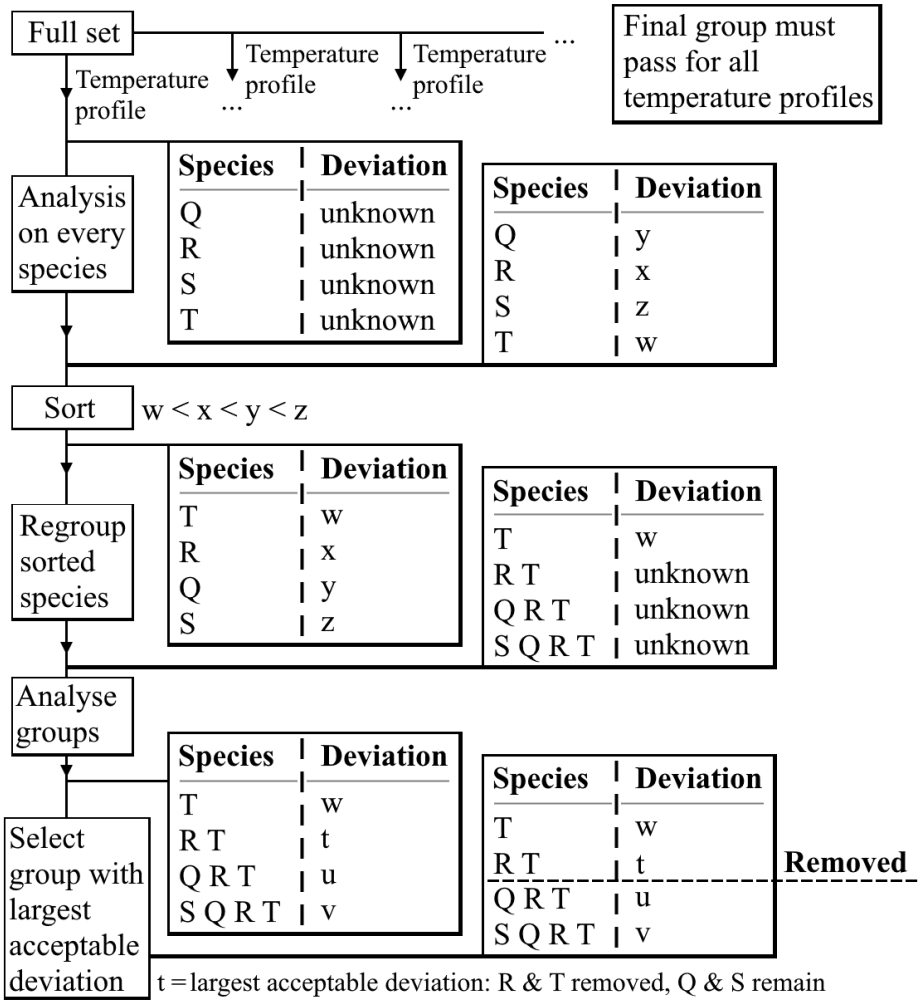

Figure S5. Reduction scheme adapted with permission from Maerivoet et al.[6] depicting the method of reduction for reactions from the full NH_3 set shown in Table S2. All rights reserved Elsevier Ltd. ©

In the paper of Maerivoet et al.[6] this reduction was first performed for species, but in our case, the set could not be reduced in terms of species, so all 13 species have to be kept in the reduced set.

This reduced set is not sufficiently stable yet for multi-dimensional modelling. Indeed, as described in numerous papers, NNH is an important intermediate compound for NH_3 cracking. However, a low potential energy barrier of 33.5 kJ/mol [24] to N_2 and H via tunneling suggests a very short calculated lifetime, in the order of 10^{-8}-10^{-10} s.[25] In a multi-dimensional model, any species which forms and is immediately destroyed, without any convective or diffusive transport to an adjacent mesh element, results in unwanted numerical instabilities. Therefore, instead of further increasing the number of mesh elements (with mesh size down to the nanometer scale), this species is removed and directly replaced with the unimolecular tunneling products N_2 and H. The effect of this change and the reduction on the chemistry is shown below.

S.5.2. Results

Figure SS6 compares the full and reduced kinetic sets (solid and dashed lines, respectively) following the reduction method for pure NH_3 decomposition at 2800 K. As the maximum allowed tolerance is set at 0.1 % absolute deviation of any species to the total molar concentration, no significant difference can be observed in Figure SS6a, which shows the molar concentrations on a linear scale. Figure SS6b depicts the molar concentrations on a logarithmic scale, where differences can be seen for the very low molar concentrations. As any thermodynamic or transport variable depends on the molar concentration of the species, the large relative error observed for the species with low concentrations is negligible for the overall plasma behavior. This is the case as long as the individual properties of a species (enthalpy, entropy, …) do not differ by orders of magnitude from all other species.

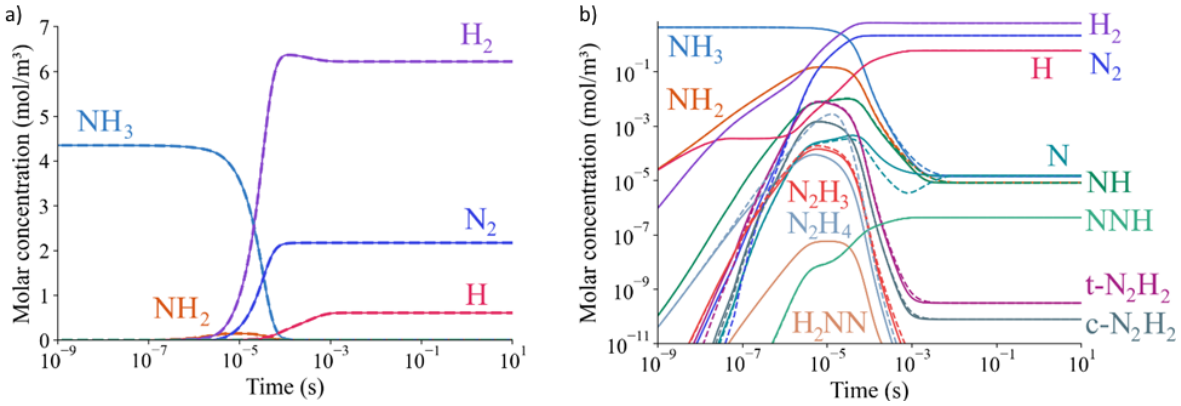

Figure S6. Molar concentration of NH_3 and (major) decomposition products, as a function of time at 2800 K, in linear (a) and logarithmic (b) scale. Full lines represent the full kinetic set, while dashed lines represent the reduced kinetic set.

As mentioned above, NNH is removed from the reduced set to avoid numerical instabilities. Figure S7 compares the full and reduced kinetic sets (solid and dashed lines, respectively), with NNH replaced by N_2 and H in the reduced set, again for pure NH_3 thermal cracking at 2800 K.

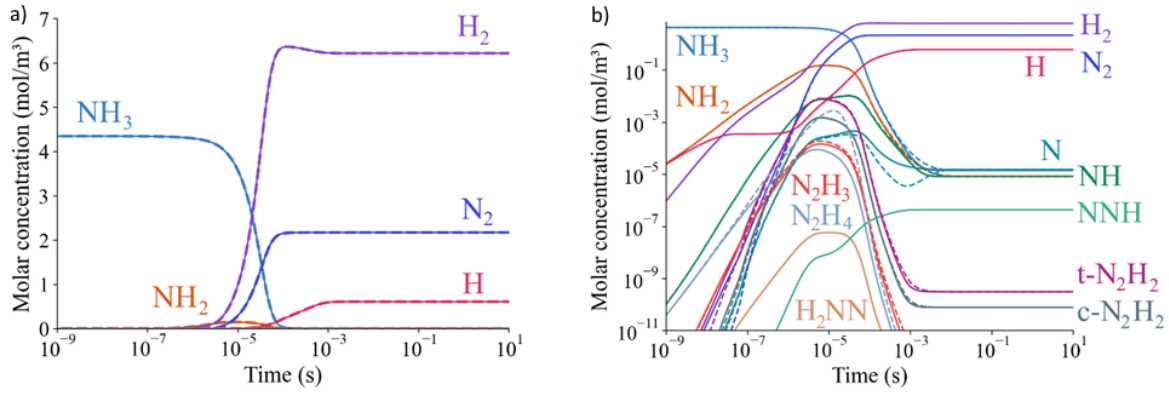

Figure S7. Molar concentration of NH_3 and (major) decomposition products, as a function of time at 2800 K, in linear (a) and logarithmic (b) scale. Full lines represent the full kinetic set, while dashed lines represent the reduced kinetic set without NNH.

We can see that the removal of NNH from the reduced set has a negligible effect on the kinetics, although NNH has a larger molar concentration than other intermediate species. This is because the destruction of NNH to N_2 and H is extremely fast, and any NNH formed is thus the result

of the detailed balanced reverse rate. The major effect of the chemistry reduction (both with and without NNH in the model) seems to be an overestimation of the N_2H_4 concentration by an order of magnitude around 10 µs. This means that we cannot use our reduced model to study the production of N_2H_4 in warm plasma, but that is not the purpose of this work. On the other hand, this overestimation has a negligible effect on the thermodynamic properties of the model, as the N_2H_4 molar concentration never exceeds 10^{-4} mol/m^3.

S.6. Reaction pathway analysis for high SEI

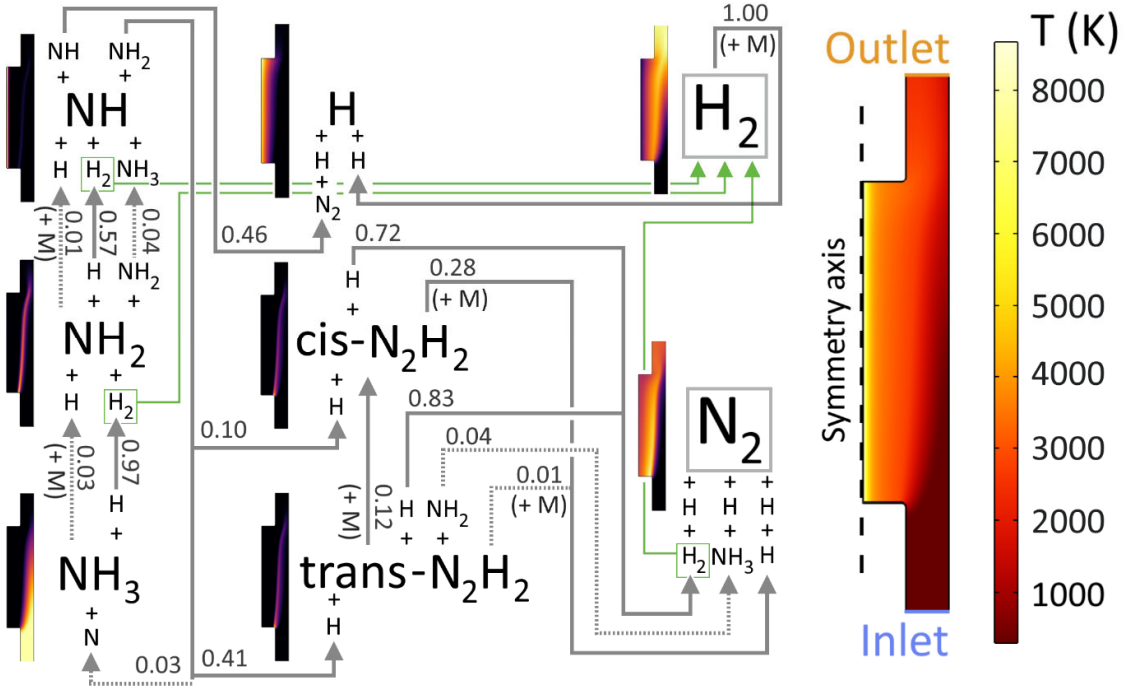

Figure S8. Reaction pathways analysis of NH_3 decomposition at 5 NLM, SEI = 231 kJ/mol. The 2D plots illustrate the mole fractions of the species, while the temperature profile is shown on the right. The arrow directions correspond to the net rates of reactions in the complete reactor. The branching ratios for the destruction of a species are denoted next to the arrows, (+ M) is shown if the reaction requires a third body as neutral collision partner to proceed. Reactions contributing to less than 10 % of the species destruction are indicated with a dashed arrow, while reactions contributing less than 1 % are omitted, for clarity. Importantly, all produced (green) H_2 molecules are linked to the final H_2 product with green arrows.

We have extrapolated our results to a much higher SEI to investigate if the same pathways are utilized in a high-power case. It must be noted that the wall temperature at this SEI is above the melting temperature of quartz glass[26]. There are three main differences between the high SEI case (Figure S8) and low SEI case (Figure 8 in the main paper). First, the decomposition of NH_3 to NH_2 in Figure 8 happens for 90 % upon reaction with H, while in Figure S8, this contribution becomes 97 %. The higher temperature in the central plasma column and larger temperature gradients at this higher SEI (cf. Figure S8) allow for 40 % more H_2 to be dissociated in the plasma center, and because H diffusion is very fast, more H atoms will reach the reactive region at higher SEI, hence the even larger contribution of H atoms to NH_3 decomposition. The same holds true, to some extent, for the decomposition of NH_2 (i.e., 57% in Figure S8 vs 53% in Figure 8).

Second, the dominant process for NH decomposition has shifted from the reaction to trans-N_2H_2 to the direct formation of N_2 upon reaction with a second NH radical, although the difference is small (45 vs 39% in Figure 8, and 41 vs 46% in Figure S8). This is an indirect effect of the higher H concentration, i.e., more H causes faster NH_2 decomposition, and thus more NH is available to react with NH instead of with NH_2.

Third, also the reactions destroying cis-N_2H_2 and trans-N_2H_2 with H have a somewhat higher contribution (72 and 83%, respectively in Figure S8, vs 62 and 77% in Figure 8), while the reactions with M, NH_2 and the isomerization reaction obviously become less important. This is once again due to the higher H fraction in the reactive region, attributed to faster diffusion.

S.7. Importance of heat source shape

In previous work[6] we used the shape of the heat source as input to the model, and it can be based on measured temperature profiles or derived from light emission shapes corresponding to the plasma region. In this work, we calculated the heat source self-consistently based on the power input and Joule heating. Here we analyze the effect of increasing the width of the heat source, from its very contracted nature originating by Joule heating (as used in this model) to a tube-filling Gaussian profile. The reason for evaluating the heat source shape is because we hypothesize the important role of H atom diffusion. If the plasma core temperature drops significantly (lower than ~3200 K) the production of H atoms is severely limited. This in turn reduces the conversion and increases the EC. The heat source was modeled as a Gaussian with a maximum at the central axis. The total deposited power was kept constant at 405 W for both heat source shapes, i.e., the power deposited by the fully coupled model for 20 NLM and SEI of 27.6 kJ/mol. The radius of the heat source is defined as the half width at half maximum. FigureS9 illustrates how the EC depends on the width of the Gaussian-shaped heat source, compared to our heat source obtained from Joule heating. Up to 1.5 mm width, the EC is more or less independent of the radius, but a larger radius leads to a significantly higher EC.

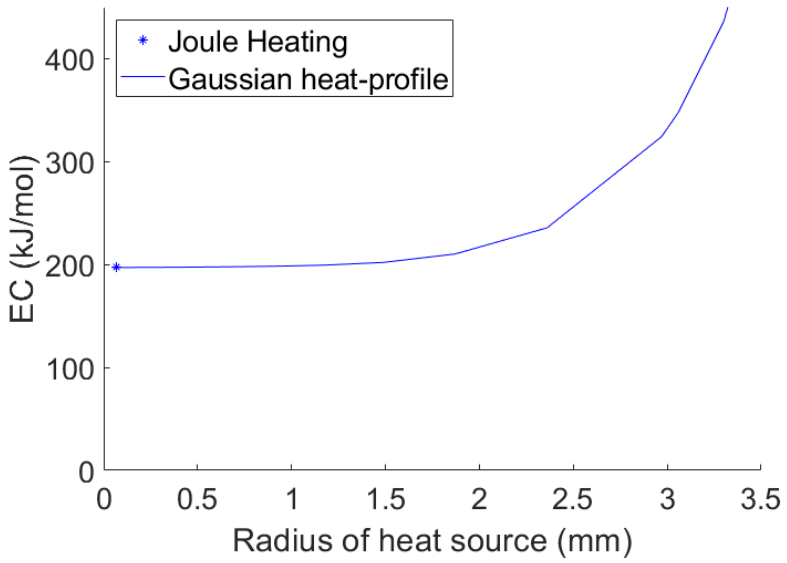

Figure S9. EC as a function of radius of the Gaussian-shaped heat source, and comparison to our heat source obtained from Joule heating, at a flow rate of 15 NLM, SEI of 29 kJ/mol and interelectrode distance of 3 cm.

FigureS10 compares the calculated temperature profiles for a Gaussian heat source width of 0.1 and 1 mm, and clearly explains why the EC (and conversion) remain almost constant when the heat source width is below 2 mm.

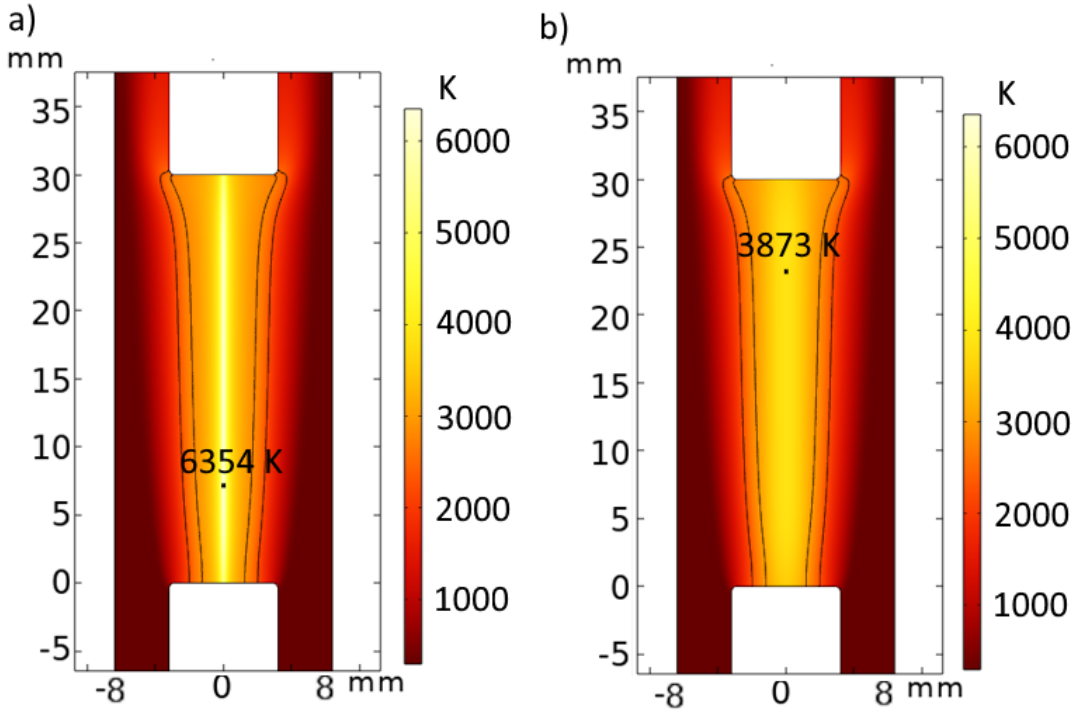

Figure S10. Temperature profile for Gaussian heat source radius of (a) 0.1 mm and (b) 1 mm, at a flow rate of 15 NLM and deposited power of 315 W. The black contour lines indicate the NH_3 decomposition rate at 1000 mol/(m^3s).

Indeed, while the central temperature drops by ca. 40 % for a heat source width of 1 mm vs 0.1 mm (i.e., 3873 K vs 6354 K; cf. Figure S10), the region where the actual chemistry happens remains broadly the same, since the chemically active region is centered around 2700 K. This is because there are no heat losses on the flat tips of the electrodes (boundaries 2 and 10 in Figure S1). Thus, all power that is deposited between r = 0 and 2 mm can only flow outwards by increasing the temperature of the gas surrounding it, or by being stored in high enthalpic products like H atoms, which diffuse away from the hot plasma column. The total amount of H atoms produced in the hot core is lower for the wide plasma (1.1 vs. 0.8 mmol/s), but the difference can still be made up by slightly increasing the maximal temperature of the chemically active zone. This compensation mechanism breaks down when the heat source no longer produces temperatures above 3200 K. This justifies the use of a heat source model, but only in the case where all chemistry happens in the plasma edge and the flow profile in the plasma does not provide a large contribution to species transport.

S.8. Transport effects 3 and 5 cm interelectrode gap

All unreacted NH_3 gas that reaches the chemically active zone must arrive via either diffusion or convection. Figure S11. shows the contribution of diffusion and convection into this zone. The diffusive flux out of this region is negligible and not shown in the figure. The effect of a limited residence time is evident by the fact that there still is a relatively large fraction of NH_3 that leaves the reactive zone via convection. i.e. not all gas that enters this zone gets converted. The definition of 'convective in', 'diffusive in' and 'convective out' are given by:

Convective in	$\iint_{T=T_c} \vec{v} \cdot \vec{n} \rho \omega_{NH_3} (\vec{v} \cdot \vec{n} > 0) dA$
Diffusive in	$\iint_{T=T_c} \vec{J}_{NH_3} \cdot \vec{n} (\vec{J}_{NH_3} \cdot \vec{n} > 0) dA$
Convective out	$\iint_{T=T_c} \vec{v} \cdot \vec{n} \rho \omega_{NH_3} (\vec{v} \cdot \vec{n} < 0) dA$

Where $\vec{J}_{NH_3}$ is defined by equation (22) in the main paper and $\vec{n}$ is the normal on the isotherm with boundary temperature T_c (2400 K).

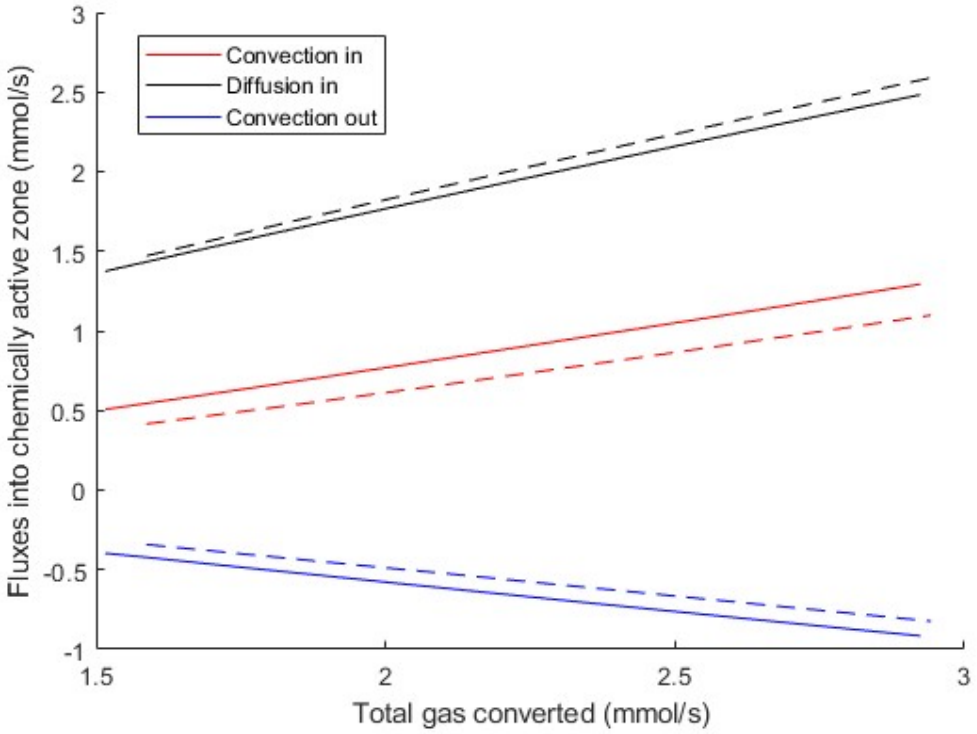

Figure S11. Contribution to total transport of the different components, solid for an interelectrode distance of 3 cm and dashed for an interelectrode distance of 5cm. See legend for color indication. The total flowrate in is 10.8 mmol/s for all cases. Total gas converted increases with increasing SEI, but as

noted in the main paper is the conversion for 3 cm and 5 cm equal for equal SEI. The range in SEI is 27-54 kJ/mol.

Figure S11 shows that a single degree of conversion (same x-position) can be obtained by different fractions of the gas 'flowing' (convective transport) into the chemically active zone (hot region). Secondly it shows the effect of residence time, if the boundary temperature was such that all gas is instantaneously cracked, then the 'convective out' term would be 0. The conversion is thus not solely determined by how much gas flows into the plasma, but by how much gas gets transported into the plasma, via either convection or diffusion.

References

(1) Churchill, S. W.; Chu, H. H. S. Correlating Equations for Laminar and Turbulent Free Convection from a Horizontal Cylinder. *International Journal of Heat and Mass Transfer* **1975**, *18* (9), 1049–1053. https://doi.org/10.1016/0017-9310(75)90222-7.

(2) COMSOL Multiphysics®. Heat Transfer Module User's Guide, 2023. https://doc.comsol.com/6.2/doc/com.comsol.help.heat/HeatTransferModuleUsersGuide.pdf.

(3) Petrov, V.; Reznik, V. Measurement of the Emissivity of Quartz Glass. *High Temperatures-High Pressures* **1972**, *v. 4*, 687–693.

(4) Naidis, G. V. Simulation of Convection-Stabilized Low-Current Glow and Arc Discharges in Atmospheric-Pressure Air. *Plasma Sources Sci. Technol.* **2007**, *16* (2), 297. https://doi.org/10.1088/0963-0252/16/2/012.

(5) Colombo, V.; Ghedini, E.; Sanibondi, P. Thermodynamic and Transport Properties in Non-Equilibrium Argon, Oxygen and Nitrogen Thermal Plasmas. *Progress in Nuclear Energy* **2008**, *50* (8), 921–933. https://doi.org/10.1016/j.pnucene.2008.06.002.

(6) Maerivoet, S.; Tsonev, I.; Slaets, J.; Reniers, F.; Bogaerts, A. Coupled Multi-Dimensional Modelling of Warm Plasmas: Application and Validation for an Atmospheric Pressure Glow Discharge in CO2/CH4/O2. *Chemical Engineering Journal* **2024**, *492*, 152006. https://doi.org/10.1016/j.cej.2024.152006.

(7) Glarborg, P.; Hashemi, H.; Marshall, P. Challenges in Kinetic Modeling of Ammonia Pyrolysis. *Fuel Communications* **2022**, *10*, 100049. https://doi.org/10.1016/j.jfueco.2022.100049.

(8) Ko, Taeho.; Marshall, Paul.; Fontijn, Arthur. Rate Coefficients for the Hydrogen Atom + Ammonia Reaction over a Wide Temperature Range. *J. Phys. Chem.* **1990**, *94* (4), 1401–1404. https://doi.org/10.1021/j100367a037.

(9) Deppe, J.; Friedrichs, G.; Ibrahim, A.; Römming, H.-J.; Wagner, H. Gg. The Thermal Decomposition of NH2 and NH Radicals. *Berichte der Bunsengesellschaft für physikalische Chemie* **1998**, *102* (10), 1474–1485. https://doi.org/10.1002/bbpc.199800016.

(10) Klippenstein, S. J.; Harding, L. B.; Ruscic, B.; Sivaramakrishnan, R.; Srinivasan, N. K.; Su, M.-C.; Michael, J. V. Thermal Decomposition of NH2OH and Subsequent Reactions: Ab Initio Transition State Theory and Reflected Shock Tube Experiments. *J Phys Chem A* **2009**, *113* (38), 10241–10259. https://doi.org/10.1021/jp905454k.

(11) Davidson, D. F.; Kohse-Höinghaus, K.; Chang, A. Y.; Hanson, R. K. A Pyrolysis Mechanism for Ammonia. *International Journal of Chemical Kinetics* **1990**, *22* (5), 513–535. https://doi.org/10.1002/kin.550220508.

(12) Whyte, A. R.; Phillips, L. F. Rates of Reaction of NH2 with N, NO AND NO2. *Chemical Physics Letters* **1983**, *102* (5), 451–454. https://doi.org/10.1016/0009-2614(83)87444-2.

(13) Li, Z.; Xie, C.; Jiang, B.; Xie, D.; Liu, L.; Sun, Z.; Zhang, D. H.; Guo, H. Quantum and Quasiclassical State-to-State Dynamics of the NH + H Reaction: Competition between Abstraction and Exchange Channels. *The Journal of Chemical Physics* **2011**, *134* (13), 134303. https://doi.org/10.1063/1.3574898.

(14) Caridade, P. J. S. B.; Rodrigues, S. P. J.; Sousa, F.; Varandas, A. J. C. Unimolecular and Bimolecular Calculations for HN2. *J. Phys. Chem. A* **2005**, *109* (10), 2356–2363. https://doi.org/10.1021/jp045102g.

(15) Tsang, W.; Hampson, R. F. Chemical Kinetic Data Base for Combustion Chemistry. Part I. Methane and Related Compounds. *Journal of Physical and Chemical Reference Data* **1986**, *15* (3), 1087–1279. https://doi.org/10.1063/1.555759.

(16) Kanno, N.; Kito, T. Theoretical Study on the Hydrogen Abstraction Reactions from Hydrazine Derivatives by H Atom. *International Journal of Chemical Kinetics* **2020**, *52* (8), 548–555. https://doi.org/10.1002/kin.21370.

(17) Gao, Y.; Alecu, I. M.; Hashemi, H.; Glarborg, P.; Marshall, P. Reactions of Hydrazine with the Amidogen Radical and Atomic Hydrogen. *Proceedings of the Combustion Institute* **2023**, *39* (1), 571–579. https://doi.org/10.1016/j.proci.2022.07.045.

(18) Diévart, P.; Catoire, L. Contributions of Experimental Data Obtained in Concentrated Mixtures to Kinetic Studies: Application to Monomethylhydrazine Pyrolysis. *J. Phys. Chem. A* **2020**, *124* (30), 6214–6236. https://doi.org/10.1021/acs.jpca.0c03144.

(19) Marshall, P.; Rawling, G.; Glarborg, P. New Reactions of Diazene and Related Species for Modelling Combustion of Amine Fuels. *Molecular Physics* **2021**, *119* (17–18), e1979674. https://doi.org/10.1080/00268976.2021.1979674.

(20) Gardiner, W. C. *Gas-Phase Combustion Chemistry*, 2nd ed.; Springer New York: New York, 1999.

(21) Hwang, D.-Y.; Mebel, A. M. Reaction Mechanism of N2/H2 Conversion to NH3: A Theoretical Study. *J. Phys. Chem. A* **2003**, *107* (16), 2865–2874. https://doi.org/10.1021/jp0270349.

(22) Pelevkin, A. V.; Sharipov, A. S. Reactions of Electronically Excited Molecular Nitrogen with H2 and H2O Molecules: Theoretical Study. *Journal of Physics D: Applied Physics* **2018**, *51* (18), 184003. https://doi.org/10.1088/1361-6463/aab97f.

(23) Cejas, E.; Mancinelli, B.; Prevosto, L. Modelling of an Atmospheric–Pressure Air Glow Discharge Operating in High–Gas Temperature Regimes: The Role of the Associative Ionization Reactions Involving Excited Atoms. *Plasma* **2020**, *3* (1), 12–26. https://doi.org/10.3390/plasma3010003.

(24) Klippenstein, S. J.; Harding, L. B.; Glarborg, P.; Miller, J. A. The Role of NNH in NO Formation and Control. *Combustion and Flame* **2011**, *158* (4), 774–789. https://doi.org/10.1016/j.combustflame.2010.12.013.

(25) Bozkaya, U.; Turney, J. M.; Yamaguchi, Y.; Schaefer, H. F., III. The Barrier Height, Unimolecular Rate Constant, and Lifetime for the Dissociation of HN2. *The Journal of Chemical Physics* **2010**, *132* (6), 064308. https://doi.org/10.1063/1.3310285.

(26) Hofmeister, A. M.; Whittington, A. G. Effects of Hydration, Annealing, and Melting on Heat Transport Properties of Fused Quartz and Fused Silica from Laser-Flash Analysis. *Journal of Non-Crystalline Solids* **2012**, *358* (8), 1072–1082. https://doi.org/10.1016/j.jnoncrysol.2012.02.012.